



## A biochar modified nickel-foam cathode with iron-foam catalyst in electro-Fenton for sulfamerazine degradation

Fengxia Deng<sup>a,b</sup>, Sixing Li<sup>b</sup>, Minghua Zhou<sup>c</sup>, Yingshi Zhu<sup>b</sup>, Shan Qiu<sup>b,\*</sup>, Kehong Li<sup>b</sup>, Fang Ma<sup>b</sup>, Jizhou Jiang<sup>d,e,\*\*</sup>

<sup>a</sup> State Key Laboratory of Urban Water Resources Center, School of Environment, Harbin Institute of Technology, Harbin, 150090, PR China

<sup>b</sup> School of Chemical and Environmental Engineering, Jianghan University, Wuhan, 430056, PR China

<sup>c</sup> Key Laboratory of Pollution Process and Environmental Criteria, Ministry of Education, College of Environmental Science and Engineering, Nankai University, Tianjin, 300350, PR China

<sup>d</sup> School of Environmental Ecology and Biological Engineering, Wuhan Institute of Technology, Wuhan, 430205, PR China

<sup>e</sup> School of Materials Science and Energy Engineering, Foshan University, Foshan, 528000, PR China

### ARTICLE INFO

#### Keywords:

Biochar  
Metal foam cathode  
Sulfamerazine (SMR)  
Polyphosphate  
Density functional theory (DFT) calculations

### ABSTRACT

A nickel-foam cathode modified by a self-nitrogen-doped biochar derived from waste giant reed was synthesized. The fabricated cathode (B@Ni-F) proved to be with high oxygen reaction reactive (ORR) reactivity and H<sub>2</sub>O<sub>2</sub> selectivity (70.41%) owing to the enrichment of oxygen functional groups and pyridinic N when low-temperature pyrolyzed biochar was incorporated. The charge transfer resistance of B@Ni-F decreased to 7.18 Ω, which was 95.7 Ω for the original nickel-foam, proving by electrochemical impedance spectroscopy (EIS). Expectedly, its H<sub>2</sub>O<sub>2</sub> accumulation improved 14 times, thus making it comparable with commonly used electrodes like carbon cloth and graphite plate. Subsequently, B@Ni-F cathode and iron-foam (Fe-F) catalyst were firstly used in the electro-Fenton (EF) process for sulfamerazine (SMR) degradation. Double-functional polyphosphate electrolytes including tetrapolyphosphate (4-TPP), tripolyphosphate (3-TPP), pyrophosphate (PP) and Na<sub>3</sub>PO<sub>4</sub> were compared with the conventional Na<sub>2</sub>SO<sub>4</sub> electrolyte in EF for SMR degradation. The absolute rate constant for oxidation of SMR by ·OH was determined to be  $(3.4 \pm 0.09) \times 10^9 \text{ M}^{-1} \text{ s}^{-1}$ . SMR degradation enhancement in the presence of polyphosphate-based electrolytes is associated with bulk ·OH generation from Fe<sup>2+</sup>-polyphosphate ligand complexes via O<sub>2</sub> activation. The Fe<sup>2+</sup>-3-TPP complexes have relatively higher oxidation ability compared to Fe<sup>2+</sup>-PP, Fe<sup>2+</sup>-PO<sub>4</sub> species. A plausible SMR oxidation pathway is proposed based on the by-products detected by UPLC-MS/MS and density functional theory (DFT) calculations. The dominant SMR degradation pathway was hydroxylation of aniline residue of SMR, followed with the cleavage of -S-N- and then breakage of aromatic rings.

### 1. Introduction

Antibiotics, important drugs for infectious diseases, have arisen concern due to the emergence of antibiotic resistant genes, bacterial transcription and their carcinogenic potential. The issue is worse in China, where many antibiotic manufacturers are sited [1–3]. Therefore, the search for ways to alleviate antibiotic environmental pollution is urgent.

Electro-Fenton (EF) is a widely used advanced oxidation process (AOPs) for the effective removal of persistence pollutants [1,4]. The main mechanism in EF is bulk ·OH generation through the classical Fenton reaction (Eq. 1), where H<sub>2</sub>O<sub>2</sub> is generated from the two-electron

oxygen reduction reaction (ORR) on cathodes (Eq. 2). In addition, the cathodic Fe<sup>2+</sup> regeneration (Eq. 3) lowers the waste iron sludge formation compared with the classical Fenton process [1,5–7]. In EF, carbonaceous-based electrodes such as carbon sponge, graphite fiber, carbon-nanotube are widely used as cathodes for H<sub>2</sub>O<sub>2</sub> production (Eq. 2) [8]. As reported previously [9,10], three-dimensional nickel-foam (Ni-F) electrode was deemed as a potential alternative cathode for scale-up applications thanks to its mechanical properties [11]. However, one limitation of Ni-F cathode is the low H<sub>2</sub>O<sub>2</sub> accumulation compared to carbonaceous electrodes although it involves H<sub>2</sub>O<sub>2</sub> production (Eqs. 4 and 5) in addition to the two-electron ORR (Eq. 2).

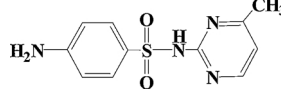
Carbon materials possess superior electrocatalytic properties to

\* Corresponding author.

\*\* Corresponding author at: School of Environmental Ecology and Biological Engineering, Wuhan Institute of Technology, Wuhan, 430205, PR China.

E-mail addresses: [qushan@hit.edu.cn](mailto:qushan@hit.edu.cn) (S. Qiu), [027wit@163.com](mailto:027wit@163.com) (J. Jiang).

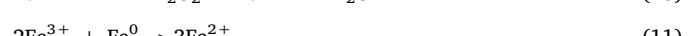
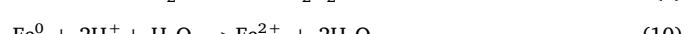
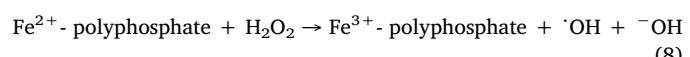
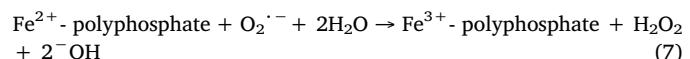
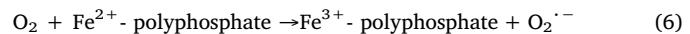
**Table 1**  
Characteristics of sulfamerazine (SMR).

Compound	Formula	Structure	Molecular weight
Sulfamerazine (SMR)	C <sub>11</sub> H <sub>12</sub> N <sub>4</sub> O <sub>2</sub> S		264.30 g mol <sup>-1</sup>

ORR, which is further enhanced by heteroatom incorporation such as N, S, P, F, etc. Various N-doped carbon materials have been used for Ni-F modification [12], among which included N-doped multi-walled carbon nanotubes [13] and N-doped porous carbon [14]. However, the preparation of those N-doped carbon involves multiple steps and harmful chemicals (such as concentrated H<sub>2</sub>SO<sub>4</sub>), thereby hindering its large-scale application. Therefore, it is highly desirable to explore a facile and eco-friendly method to obtain N-doped carbon for Ni-F decoration, aiming for H<sub>2</sub>O<sub>2</sub> generation improvement. In recent years, renewable and low-cost biomass such as water hyacinth [15], reed [16], fungi [17], long bean [18] has been used as carbon precursors, where nitrogen-containing biomass are endowed as a desirable precursor of N-enriched porous carbon with excellent properties [15,16]. Biochar with highly-perfect graphitization, porous structure along with the enriched functional groups effectively facilitates the electron transport and the electrochemical utilization [19,20]. Its surface properties such as functional groups, large surface area endow biochar to remove persistence pollutants following mechanisms of electrostatic attraction, π-π stacking, hydrogen bonding, chemisorption and pore-filling [21,22]. Giant reed (*Arundo donax* L.), a wetland plant widely grown in the south part of China, was deemed as an appropriate feedstock for biochar generation owing to high yields, reaching 45 tons per hectare [23,24]. Moreover, it mainly composed of cellulose, lignin and hemicellulose with abundant polar hydroxyl and carbonyl groups. Nevertheless, limited investigations have been reported on Ni-F modification with N-doped porous carbon derived from sustainable giant reed biomass. In this study, nitrogen-enriched giant reed grown in eutrophic water as the precursor of self-nitrogen-doped biochar for Ni-F cathode modification.

In our previous investigations, we have reported that double-functional polyphosphate supporting electrolytes such as tetrapolyphosphate (4-TPP), tripolyphosphate (3-TPP) and pyrophosphate (PP) was able to circumvent pH-limited effect on EF [25,26]. Because those electrolytes form stable Fe-polyphosphate complexes with iron ions at a wide pH range in solution. Importantly, those complexes enhance the formation of ·OH through the activation of O<sub>2</sub> according to Eqs. 6–8 [25,26]. However, there is a lack of a comparison between these polyphosphate electrolytes in EF regarding pollutant degradation such as 4-TPP, 3-TPP, PP and Na<sub>3</sub>PO<sub>4</sub>.

Considering various sulfamerazine (SMR) treatments by electrochemical techniques [27], as far as we know, little research work has attempted to conduct SMR degradation through EF. Therefore, in this study, we aim: 1) to develop a self-nitrogen-enriched biochar coated on Ni-F (B@Ni-F) through waste green reed biomass and to assess its performance on H<sub>2</sub>O<sub>2</sub> accumulation; 2) to investigate SMR degradation in EF with B@Ni-F cathode and the iron-foam (Fe-F) catalyst, where Fe-F catalyst provides Fe<sup>2+</sup> ions via chemical corrosion (Eqs. 9–11); 3) to compare SMR degradation using 4-TPP, 3-TPP, PP, Na<sub>3</sub>PO<sub>4</sub> and Na<sub>2</sub>SO<sub>4</sub> supporting electrolytes; 4) to propose a possible SMR degradation pathway in EF by UPLC-MS/MS as well as density functional theory (DFT) calculations.



## 2. Materials and methods

### 2.1. Chemicals and materials

Sulfamerazine (SMR, purity > 99%, CAS 127-79-7) (Table 1), tetrapolyphosphate (4-TPP, purity > 95%, CAS 14986-84-6), tripolyphosphate (3-TPP, purity > 95%, CAS 7758-29-4), pyrophosphate (PP, purity > 95%, CAS 14000-31-8) and Na<sub>3</sub>PO<sub>4</sub> (purity > 95%, CAS 7601-54-9), p-benzoquinone (BQ) and benzoic acid (BA) were reagent grade from Sigma-Aldrich, China. Acetonitrile, H<sub>3</sub>PO<sub>4</sub> and formic acid were HPLC grade, supplying from Dikma Technologies Inc. The detail characterization of iron-foam (Fe-F) catalyst was reported in our previous investigation [26].

### 2.2. Fabrication of B@Ni-F cathode

Giant reed (GR) was collected, washed and sliced into small pieces, followed with drying in a chamber at 100 °C. The two-steps pyrolysis method was used to obtain a high-strength, porosity and high yield biochar [28]. The details were illustrated as follows: initially pre-carbonation in ambient air at 260 °C for 6 h with a heating ramp 10 °C min<sup>-1</sup>, then followed a complete pyrolysis at 500 °C with a heating rate of 5 °C min<sup>-1</sup> in quartz tube furnace under a continuous nitrogen gas flow (150 mL min<sup>-1</sup>) and stabilized for 2 h. The prepared biochar was coated on the Ni-F using the method reported previously by our group [14].

### 2.3. Characterization of B@Ni-F cathode

Characterization of cathodes including morphology, surface elemental composition and functional groups bonding environment was conducted using Scanning-Electron-Microscopy (Zeiss SUPRA 55 SAPPHIRE), X-ray photoelectron spectroscopy (XPS, ThermoFisher ESCALAB 250Xi, USA) and Fourier transform infrared (FT-IR, Perkin Elmer infrared spectrometer), while details were given in supporting information (SI. 1). Contact angle measurements on the electrode surface were conducted on the optical system (VAF-30, China) at room temperature. Ultraviolet photoemission spectroscopy (UPS) measurements were performed with an unfiltered He I (21.2 eV) gas discharge lamp and a total instrumental energy resolution of 100 meV. The Fermi level E<sub>F</sub> is located at E = 0 which was measured from the Fermi edge of

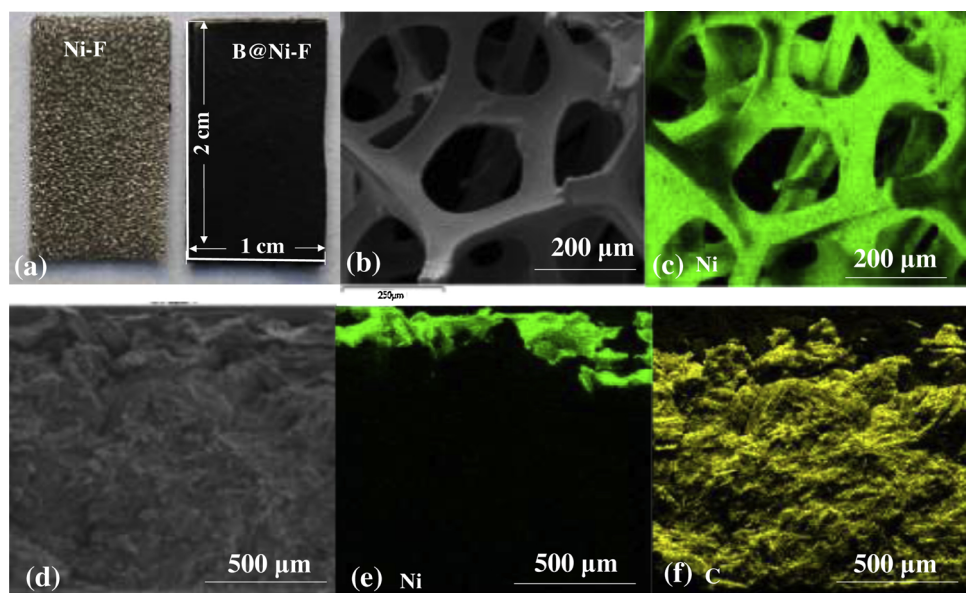


**Fig. 1.** SEM micrographs of Ni-F (a), (b), (c) and B@Ni-F (d), (e), (f) cathodes.

an evaporated Ag film. To characterize its electrochemical properties of oxygen reduction reaction (ORR), charge transfer resistance and the electron transfer number (*n*) involving ORR, the linear sweep voltammetry (LSV), electrochemical impedance spectroscopy (EIS) and rotating disk electrode (RDE) measurement were used and the conditions were given in SI. 1. The Koutecky-Levich (K-L) equation (Eq. 12) was used to calculate the *n* during ORR [29].

$$1/J = 1/J_K + 1/(0.2nFC_{O_2}D_{O_2}^{2/3}\nu^{-1/6}\omega^{1/2}) \quad (12)$$

Where *J* is the measured current density ( $\text{mA cm}^{-2}$ ), *J<sub>K</sub>* is the kinetic current density, *n* is the number of electrons transferred, *F* is the Faraday constant ( $96,485 \text{ C mol}^{-1}$ ), *C<sub>O<sub>2</sub></sub>* is the bulk oxygen concentration ( $1.2 \times 10^{-6} \text{ mol cm}^{-3}$ ), *D<sub>O<sub>2</sub></sub>* is the diffusion coefficient of oxygen ( $1.9 \times 10^{-5} \text{ mol cm}^{-3}$ ), *v* is the kinematic viscosity of the solution ( $0.01 \text{ cm}^2 \text{ s}^{-1}$ ) and *ω* is the rotating rate (rpm).

#### 2.4. Assessment of B@Ni-F cathode for $H_2O_2$ accumulation

The same reactor reported previously [26] was used for  $H_2O_2$  accumulation, where a Pt foil ( $1 \text{ cm} \times 2 \text{ cm}$ ) was applied as the anode and the same size of Ni-F/B@Ni-F/carbon cloth/graphite plate were used as cathodes. Current efficiency (CE) regarding  $H_2O_2$  generation was deduced according to Orlando's report [30].

#### 2.5. Assessment of B@Ni-F cathode performance for SMR degradation in EF

SMR degradation/mineralization was performed using the same reactor, while  $1 \text{ g L}^{-1}$  Fe-F catalyst was used as the catalyst for providing iron ions. SMR was measured via Ultra-High Performance Liquid Chromatography (UPLC) approach with a chromatographic peak at a retention time of 2.75 min [31].

The generation of ·OH was quantified using terephthalic acid (TA) photoluminescence method (PL), where the highly reactive TA exclusively captured ·OH to form fluorescent 2-hydroxyterephthalic acid (TAOH), emitting a unique fluorescence at 429 nm [32]. The sample was analyzed by a fluorescence spectrometer (F-2700, Hitachi, Japan) at an excitation wavelength of 315 nm. Moreover, electron paramagnetic resonance (EPR) spectra (a Bruker A300 EPR spectrometer) were used to detect the free radicals with 5, 5-dimethyl-1-pyrroline-N-oxide (DMPO) as the hydroxyl radical trapper.

Competitive kinetics experiment was carried out to determine the

absolute rate constant of SMR ( $k_{abs(SMR)}$ ) degradation by ·OH according to the following equation (Eq. 13), using benzoic acid (BA) as a competitor for ·OH with the well-known  $k_{abs(BA)} = (5.91 \pm 0.54) \times 10^9 \text{ M}^{-1} \text{ s}^{-1}$  [33]. The method for SMR measurement was used for BA, BQ detection with a retention time of 3.22 min and 2.48 min, respectively.

$$k_{abs(SMR)} = k_{abs(BA)} \times (k_{app(SMR)/k_{app(BA)}}) \quad (13)$$

Where  $k_{abs(SMR)}$ ,  $k_{abs(BA)}$  are the absolute rate constant of SMR and BA with ·OH, while  $k_{app(SMR)}$  and  $k_{app(BA)}$  are the apparent rate constant.

Furthermore, a general SMR oxidation route was suggested according to the identified intermediates including aromatic by-products, short-chain acids and released  $\text{NO}_3^-$ ,  $\text{SO}_4^{2-}$ ,  $\text{NH}_4^+$  detected by UPLC-MS/MS, UPLC and ion chromatography, where the analysis parameters were described in supporting information (SI. 2). Toxicity evolution of SMR degradation by EF was investigated based on the standard OIN 11348-3 and the analysis details were given in SI. 2.

#### 2.6. Theoretical calculations

The geometry structures, frequencies, summary of electronic and thermal energies of SMR coupled with the corresponding products were performed with Gaussian09 software package on an Intel Pentium PC computer with 3.50 GHz processor and 64 GB of memory (SI. Reference [2]). Optimization of the molecular structures were conducted by means of density functional theory (DFT) with the Becke's 3 parameters and the Lee-Yang-Parr's nonlocal correlation functional (B3LYP). The basis sets for C, N, S, O and H were 6-31G(d) with diffuse function for N, S and O atoms. The average local ionization energy (ALIE) and quantitative three-dimensional (3D) electrostatic potential (ESP) mapping images were calculated using Multiwfn (v 3.4) and plotted by VMD programs (v 1.9.3).

### 3. Results and discussion

#### 3.1. Characterization of B@Ni-F cathode

**Fig. 1a** showed the morphology of Ni-F and B@Ni-F cathodes, where nickel evenly distributed on the surface of the porous three-dimensional structure of original Ni-F (**Fig. 1b** and **c**). After modification, B@Ni-F with a biochar loading of  $0.5 \text{ g cm}^{-2}$  was covered by a dense biochar layer (**Fig. 1d**). Apart from Ni base (**Fig. 1e**), it was mainly composed of C element (**Fig. 1f**). Those biochar layers were made of small particles

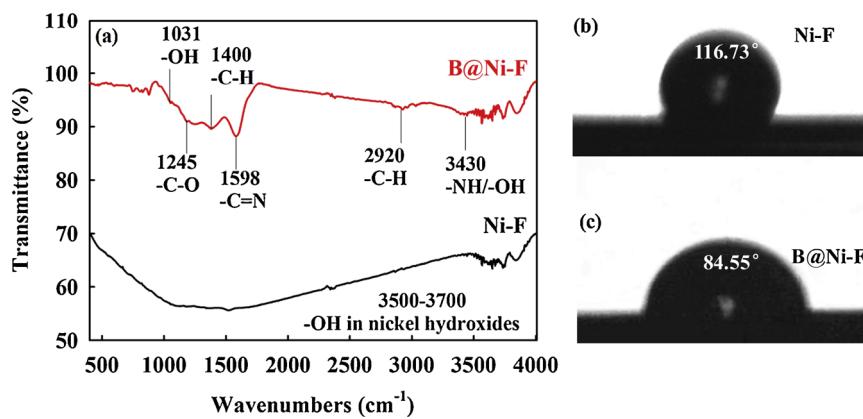


Fig. 2. FTIR spectra of cathodes (a) and the corresponding contact angles (b–c).

approximately 40–50 nm, when observed at higher magnification times (Fig. SI. 1a, b). Approximately 15% (atomic percentage) oxygen and 5% nitrogen was introduced on B@Ni-F cathode since low-temperature biochar favored oxygen/nitrogen functional groups conservation during the pyrolysis process (Fig. SI. 1c, d).

According to previous report [34], a band ranged from 3500–3700  $\text{cm}^{-1}$  was associated with –OH vibration showed in the FTIR of Ni-F cathode (Fig. 2a). After modification with biochar, B@Ni-F was enriched with oxygen and nitrogen functional groups, as evidenced by FT-IR showed in Fig. 2a. The bands at 1031  $\text{cm}^{-1}$ , 1245  $\text{cm}^{-1}$ , 1400  $\text{cm}^{-1}$ , 2920  $\text{cm}^{-1}$  were assigned to the –OH bending, the –C=O stretching vibrations, –C–H bending, –C–H stretching, respectively due to the oxygen functional groups incorporated with biochar [35,36]. The nitrogen functional groups were confirmed by the appearance of the following peaks: 3430  $\text{cm}^{-1}$  (–N–H stretching vibration) and 1598  $\text{cm}^{-1}$  (–C=N groups' stretching vibration) [37,38]. The oxygen containing functional groups (–C=O) favors  $\text{H}_2\text{O}_2$  selectivity improvement [39]. In addition, the successful introduction of surface functional oxygen/nitrogen groups increased the hydrophilicity of the cathode, decreasing the contact angle from 116.73° (Fig. 2b) of Ni-F to 84.55° (Fig. 2c), which was in accordance with previous studies [15].

As revealed by XPS results in Fig. SI. 2, the appearance of N1s on B@Ni-F cathode further confirmed nitrogen introduction, which was in accordance with SEM and FTIR results. The high-resolution C1s deconvoluted spectra of B@Ni-F included as follows (Fig. 3a): 284.5 eV for C–C/C–H/C=C, 285.6 eV for C–N/C=N, 286.1 eV for C–O and 288.7 eV for –COOH [40,41], while the binding energy of 398.07 eV and 399.1 eV proved the incorporation of the pyrrolic N (62.05%) and pyridinic N (37.95%) (Fig. 3b) [42]. Therefore, the introduction of pyridinic N on B@Ni-F cathode was favorable for  $\text{H}_2\text{O}_2$  generation since Nakamura group confirmed carbon atoms next to pyridinic N was the active sites for ORR through tunnelling oxygen chemisorption mode [43].

### 3.2. Electrochemical characterization of B@Ni-F cathode

The electrochemical properties for ORR were performed by LSV, EIS and RDE. As shown in Fig. 4a that ORR occurred on both cathodes since the current density was much higher in  $\text{O}_2$ -saturated solution than that in  $\text{N}_2$ -saturated electrolyte. Expectedly, an enhancement of electroactive surface area was achieved, revealing from a more pronounced net current on B@Ni-F compared with the raw Ni-F. It confirmed that ORR reactivity on B@Ni-F cathode was higher compared with Ni-F. Therefore, it gave a hint that a plausible improvement of  $\text{H}_2\text{O}_2$  via two-electron ORR through providing more active electrochemical sites [30]. As reported previously [14], the charge transfer reaction resistance dominated at the Ni-F cathode since a semicircle at frequency ranged 0.01 Hz and 100 kHz was obtained, revealing from EIS results in Fig. 4b. For the modified B@Ni-F cathode, a smaller semicircle was observed in

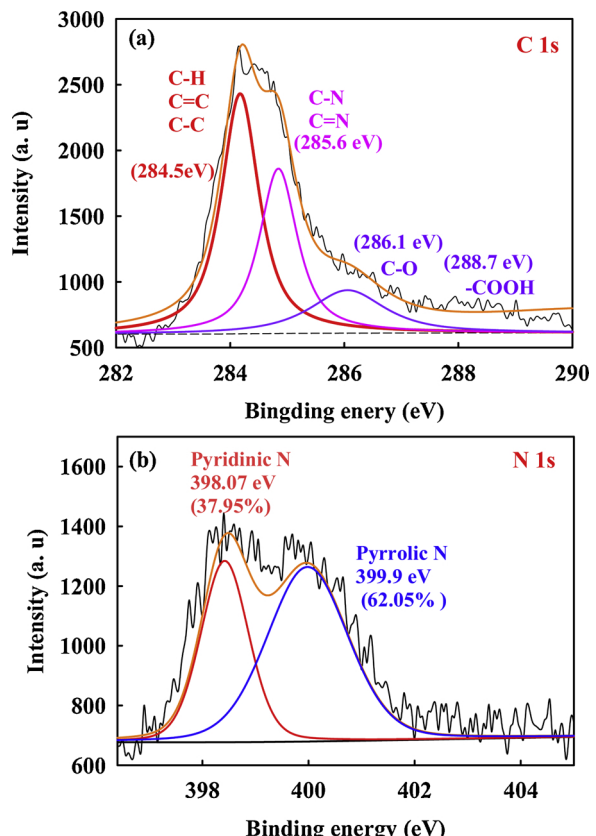


Fig. 3. XPS spectra of C1s deconvolution (b) and N1s deconvolution of B@Ni-F cathode.

high frequency followed with a bigger semicircle attributed to adsorption\desorption of adsorbed species. The fitting equivalent circuit (Fig. SI. 3a) of Ni-F EIS curve was given as follows: a charge transfer resistance ( $R_p$ ) in parallel with a constant phase element (CPE) coupled with an electrolyte resistance ( $R_s$ ). However, another R and CPE (represented the adsorption\desorption element) were comprised in the circuit after biochar introduction as shown in Fig. SI. 3b [44]. The appearance of adsorption\desorption ability was in accordance with its nature as adsorbent due to the presence of oxygen/nitrogen functional groups and larger surface area [45]. The charge transfer resistance ( $R_p$ ) decreased from 95.7  $\Omega$  on raw nickel electrode to 7.18  $\Omega$  after biochar-coating, suggesting an improvement of ORR and hence the current efficiency. In addition, RDE technique was used in this section to assess the reaction mechanism of the electron transfer process on B@Ni-F cathode. It presented in Fig. 5a that current density rose with the

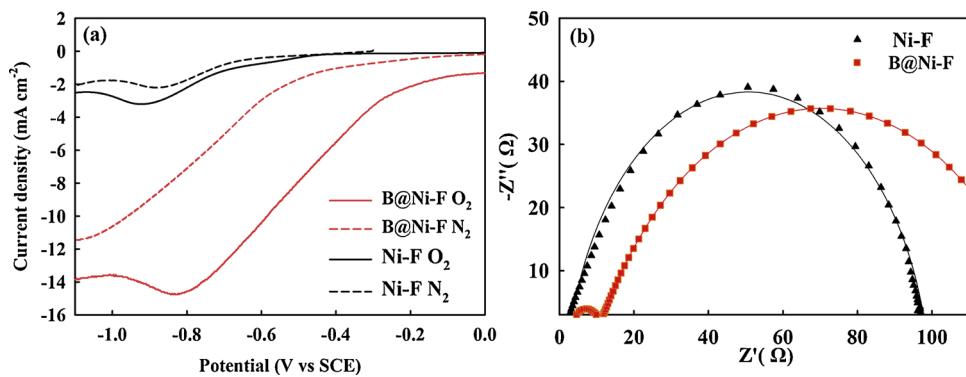


Fig. 4. LSV curves of both cathodes in N<sub>2</sub>/O<sub>2</sub>-saturated solution (a), Nyquist plots of Ni-F and B@Ni-F (b).

rotation speed owing to a shorten diffusion layer [46]. The linearity of the K-L plot at different potentials meant first-order kinetics regarding ORR [47]. Moreover, the number of electron transfer at different potentials were calculated to be around 2 according to K-L plots in Fig. 5b, suggesting a favorable 2-electron reduction toward ORR to generate H<sub>2</sub>O<sub>2</sub>.

### 3.3. Biochar loading optimization and its comparison with commonly used cathodes on H<sub>2</sub>O<sub>2</sub> accumulation

#### 3.3.1. Biochar loading optimization

The optimal biochar loading on Ni-F was firstly investigated at a fixed current density of 10 mA cm<sup>-2</sup> and H<sub>2</sub>O<sub>2</sub> accumulation was illustrated in Fig. 6, where it can be seen that the highest H<sub>2</sub>O<sub>2</sub> accumulation was achieved (1349.78 μM in 40 min) with a biochar amount of 0.5 g cm<sup>-2</sup> modified on Ni-F. H<sub>2</sub>O<sub>2</sub> accumulation obtained with the raw biochar electrode was only 94.89 μM, which was in agreement with previous investigation [48] despite the fact that Ni-F, a three-dimensional structure electrode, favors mass transfer and has good conductivity. Interestingly, a low H<sub>2</sub>O<sub>2</sub> accumulation (391.53 μM) was observed on the raw biochar electrode. As of note, the biochar used for coating was pyrolyzed at a relative low temperature (500 °C), hoping to conserve surface oxygen functional groups, which was the active site for 2e- ORR [49]. However, the conductivity of the low-carbonized biochar was not satisfactory and then it led to a relative low ORR reactivity. As biochar was coated on Ni-F, H<sub>2</sub>O<sub>2</sub> accumulation improved from 391.53 μM to 1349.78 μM since the conductivity issue was resolved with Ni-F assistance. However, a biochar loading higher than 0.5 g cm<sup>-2</sup> was not suitable because a dense layer generated by PTFE content would hinder mass transfer and then ORR [50]. Consequently, the biochar loading of 0.5 g cm<sup>-2</sup> was chosen for the following investigation.

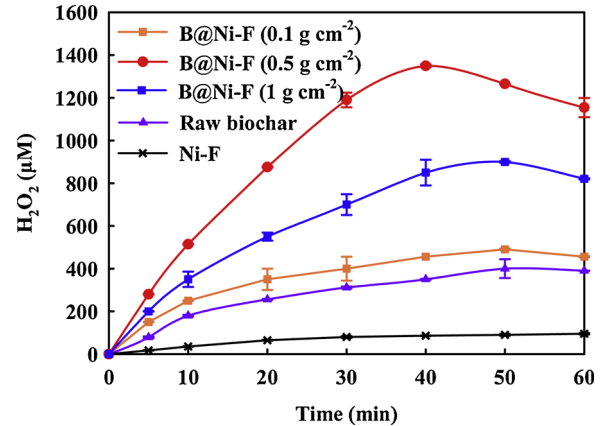


Fig. 6. H<sub>2</sub>O<sub>2</sub> accumulation on B@Ni-F cathode with different biochar loading.

#### 3.3.2. Comparison with commonly used cathodes regarding H<sub>2</sub>O<sub>2</sub> generation

Despite the above-mentioned characterization results demonstrated an ORR enhancement of B@Ni-F cathode, a direct proof should be given regarding H<sub>2</sub>O<sub>2</sub> accumulation since it determines the efficiency of EF process. Therefore, H<sub>2</sub>O<sub>2</sub> accumulation ability on both cathodes was compared in Fig. 7a. Approximately 14 times of H<sub>2</sub>O<sub>2</sub> accumulation enhancement was achieved, rising from 94.89 μM to 1154 μM during 40 min electrolysis after biochar coating on Ni-F, confirming the effective modification. A gradual decrease of H<sub>2</sub>O<sub>2</sub> accumulation was attributed to its decomposition in the bulk (Eq. 14) along with electrode surface decomposition reactions (Eqs. 15 and 16).

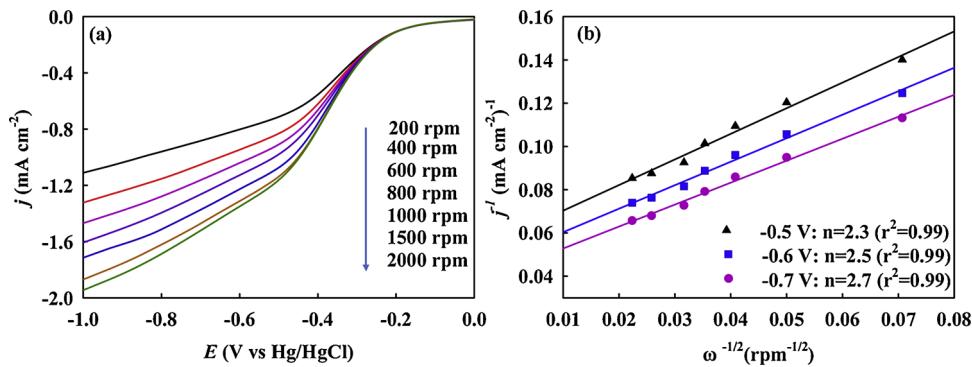
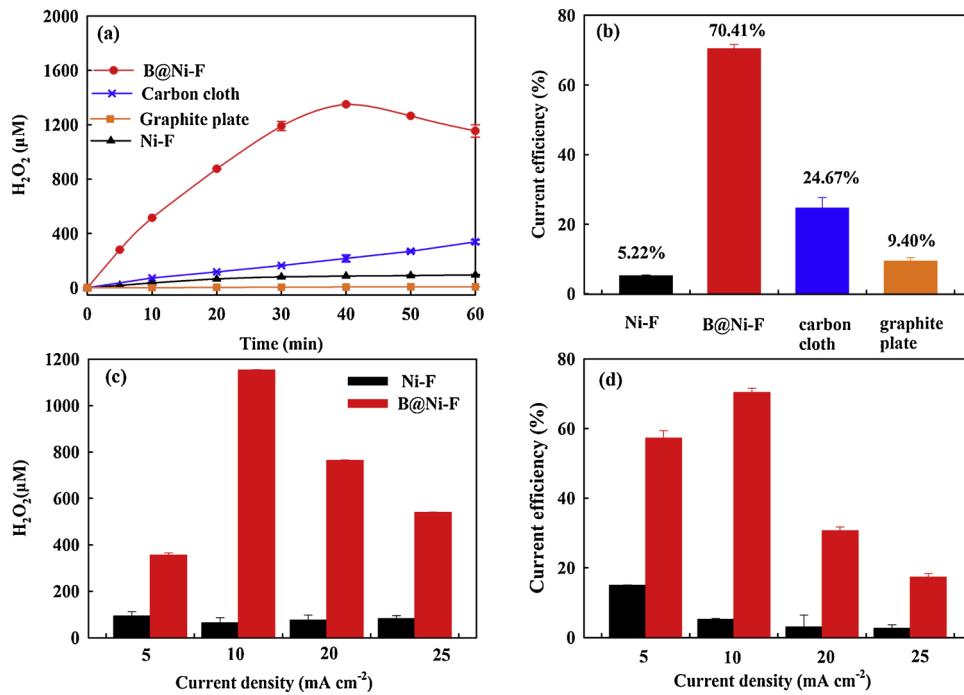
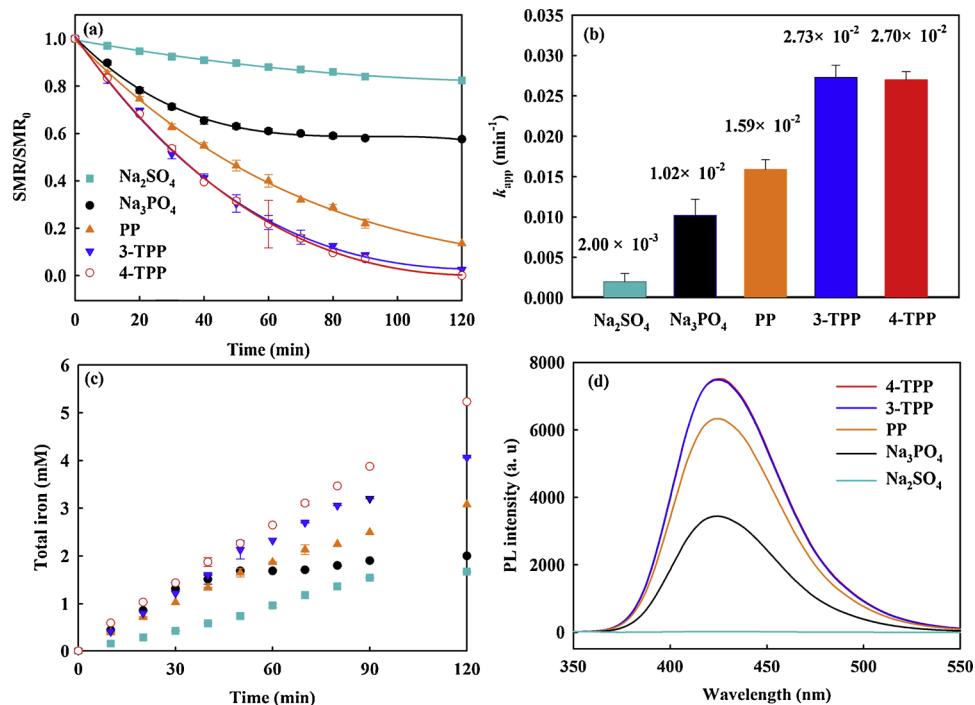


Fig. 5. LSV for B@Ni-F at different rotating speeds in O<sub>2</sub>-saturated electrolyte (a) and the corresponding Koutecky-Levich plots ( $j^{-1}$  vs  $\omega^{-1/2}$ , where  $j$  is the current density in A m<sup>-2</sup> and  $\omega$  is the rotating speed in rpm) (the number of electron number between potential -0.5 V and -0.8 V was insert into (b).



**Fig. 7.** H<sub>2</sub>O<sub>2</sub> accumulation comparisons among different cathodes (a), the related CE at 20 min electrolysis (b), influence of current density on H<sub>2</sub>O<sub>2</sub> accumulation (c), and CE on both cathodes at 20 min electrolysis (d). Conditions: pH = 3, [Na<sub>2</sub>SO<sub>4</sub>] = 50 mM, air flow rate = 500 mL min<sup>-1</sup>.



**Fig. 8.** SMR degradation by EF using different supporting electrolytes (a), a pseudo first-order kinetic rate constant comparison (b), the released total iron (c) and PL spectra of TAOH for EF with different supporting electrolytes (d). Conditions: [SMR] = 50 mg L<sup>-1</sup>, pH = 6, air flow rate = 500 mL min<sup>-1</sup>, I = 10 mA cm<sup>-2</sup>.



In addition, its H<sub>2</sub>O<sub>2</sub> generation capacity coupled with current efficiency (70.41% at 20 min) outcompeted the widely used graphite and carbon cloth, as demonstrated in Fig. 7a–b. Further, normalized H<sub>2</sub>O<sub>2</sub> accumulation to cathode's geometrical area, the specific H<sub>2</sub>O<sub>2</sub> accumulation on B@Ni-F cathode was 577 μM h<sup>-1</sup> cm<sup>-2</sup>. This value was higher than previously reported carbon-coated Ni-F [13], carbon-PTFE gas diffusion electrode [51] and long bean biochar [15].

The influence of applied current density on H<sub>2</sub>O<sub>2</sub> generation and CE was investigated in Fig. 7c–d. It showed H<sub>2</sub>O<sub>2</sub> concentration and CE on the modified cathode excelled in the raw Ni-F cathode during the whole current density investigated, again confirming the effectiveness of this biochar coating. As applied current density increased from 5 mA cm<sup>-2</sup> to 10 mA cm<sup>-2</sup>, H<sub>2</sub>O<sub>2</sub> concentration experienced an obvious rise, increasing from 356.16 μM to 1154 μM with CE of 57.24% and 70.41%, respectively. Nevertheless, a sharp drop of H<sub>2</sub>O<sub>2</sub> accumulation (763.73 μM) along with a lower CE (30.70%) was obtained when

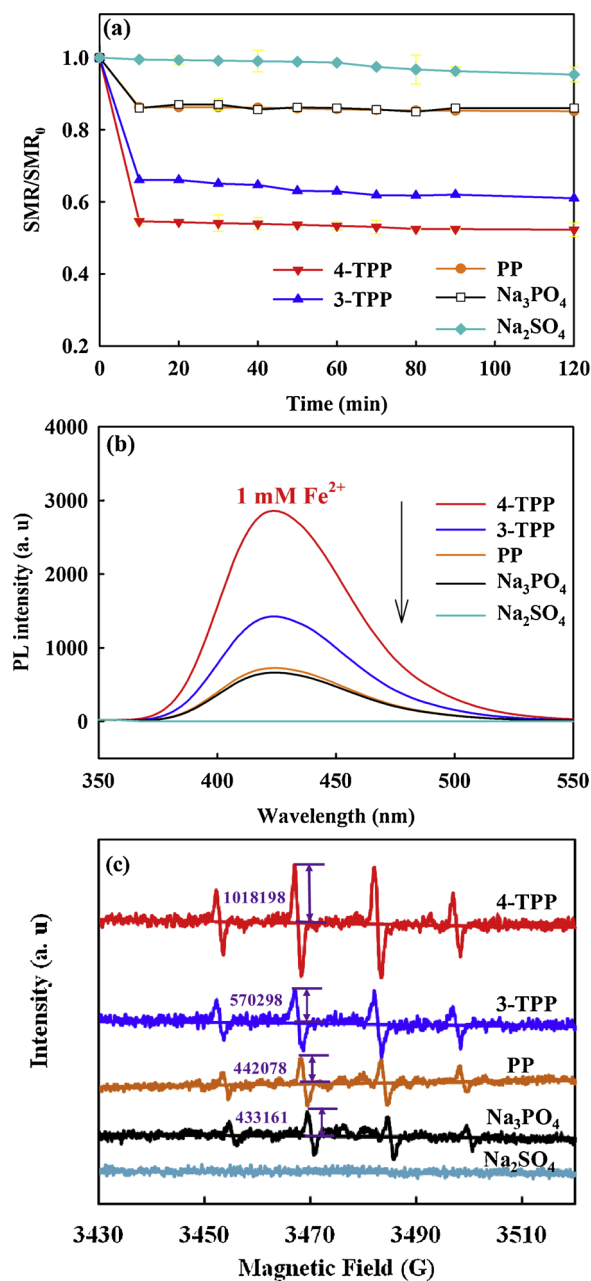


**Fig. 9.** SMR degradation in different  $\text{Fe}^{2+}$ -Ligands systems in the absence of current (a), PL spectra of TAOH for different  $\text{Fe}^{2+}$ -ligands and ESR spectra of various  $\text{Fe}^{2+}$ -ligand complexes (c). Conditions: pH = 6,  $\text{Fe}^{2+}$  = 1 mM, air flow rate = 500 mL min<sup>-1</sup>, [electrolyte] = 50 mM, pH = 6.

current reached 20 mA cm<sup>-2</sup>, which was mainly attributed to the enhancement of  $\text{H}_2\text{O}_2$  decomposition reaction [14].

#### 3.4. Mechanism of ORR activity and $\text{H}_2\text{O}_2$ selectivity enhancement involving biochar-coating

$\text{H}_2\text{O}_2$  generation ability on B@Ni-F improved 14 times compared with raw Ni-F cathode as a self-N-doped biochar introduction, confirming the significant role of biochar during  $\text{H}_2\text{O}_2$  accumulation. Mechanisms involved improvement of  $\text{H}_2\text{O}_2$  formation and its selectivity (70.41%) were attributed to the following points: i) As of note, oxygen functional groups are recently recognized as the active sites for two-electron ORR and are positively correlated with selectivity of  $\text{H}_2\text{O}_2$  production [39,49,52]. Consequently, low-temperature pyrolyzed biochar favored  $\text{H}_2\text{O}_2$  selectivity improvement due to a better conservation

of surface oxygen functional groups like  $-\text{C}=\text{O}$  and  $\text{C}-\text{O}-\text{C}$ , etc. at a lower carbonization temperature (Table. SI.1). ii) Heteroatom doping, concretely, N-doping have been intensively confirmed as an effective strategy to boost ORR reactivity [49]. The incorporation of pyrrolic N (62.05%) and pyridinic N (37.95%) (Fig. 3b) derived from the self-nitrogen containing waste giant reed biomass might be responsible for ORR reactivity improvement. In addition, the incorporation of biochar with a porous structure and then an enhancement of electroactive surface area reduced the charge transfer resistance (Fig. 4b), favoring ORR reactivity. iii) Potentially, a synergy between oxygen functional groups and -N-C active sites contributed simultaneously to the high  $\text{H}_2\text{O}_2$  generation, a similar synergistic effect between Co-N<sub>x</sub>-C sites and oxygen functional groups for boosting  $\text{H}_2\text{O}_2$  electrosynthesis has been proved recently [49]. Therefore, the oxygen functional groups and -N-C active sites co-modified on B@Ni-F via a facile carbonized self-nitrogen containing waste giant reed biomass, favoring the reactivity and selectivity of ORR for  $\text{H}_2\text{O}_2$  production.

#### 3.5. SMR degradation in EF using B@Ni-F cathode and Fe-Foam catalyst

##### 3.5.1. Polyphosphate-based supporting electrolyte optimization

Supporting electrolyte, on one hand, determines ohmic overpotential and energy consumption for the electrochemical process [53]. On the other hand, unconventional polyphosphate-based electrolytes, such as 4-TPP, 3-TPP and PP (the molecular structures as shown Fig. SI. 4) could enhance the oxidation ability of EF through their Fe-polyphosphate compounds via oxygen activation to generate ·OH (Eqs. 6–8) [25,54]. Nevertheless, comparisons among those polyphosphate-based electrolytes regarding pollutant degradation in EF have not been reported yet. As a consequence, various supporting electrolytes, including Na<sub>2</sub>SO<sub>4</sub>, Na<sub>3</sub>PO<sub>4</sub>, PP, 3-TPP and 4-TPP were compared in terms of SMR degradation in EF under the following conditions according to previous investigation [26]: 1 g L<sup>-1</sup> Fe-F catalyst, pH = 6, supporting electrolyte = 50 mM, I = 10 mA cm<sup>-2</sup>.

It shows from Fig. 8a that SMR degradation experienced a dramatic increase with 43%, 87%, 100%, 100% for Na<sub>3</sub>PO<sub>4</sub>, PP, 3-TPP and 4-TPP electrolyte in contrast with conventional Na<sub>2</sub>SO<sub>4</sub> electrolyte (18% in 2 h). In all cases, the SMR degradation obeyed a first-order kinetic with an apparent rate constant ( $k_{\text{app}}$ ) of  $2.00 \times 10^{-3}$  min<sup>-1</sup> for Na<sub>2</sub>SO<sub>4</sub>, which was approximately 12.50 timers lower than that of 4-TPP ( $2.70 \times 10^{-2}$  min<sup>-1</sup>), 12.65 timers lower than that of 3-TPP ( $2.73 \times 10^{-2}$  min<sup>-1</sup>), 6.95 timers lower than that of PP ( $1.59 \times 10^{-2}$  min<sup>-1</sup>) and 5.1 times lower than that of Na<sub>3</sub>PO<sub>4</sub> ( $1.02 \times 10^{-2}$  min<sup>-1</sup>) (Fig. 8b). It confirmed the superiority of polyphosphate-based electrolytes in EF for SMR treatment compared to the conventional electrolyte (Na<sub>2</sub>SO<sub>4</sub>).

To assess the mechanism of different SMR decays among these electrolytes, oxidation ability of newly formed  $\text{Fe}^{2+}$ -ligands (ligand stood for 4-TPP, 3-TPP, PP, PO<sub>4</sub>) should be taken into consideration since those complex were able to activate oxygen to form  $\text{H}_2\text{O}_2$  and ·OH species [25,44]. As a consequence, SMR decay experiment by various  $\text{Fe}^{2+}$ -ligands in oxygen-saturated solution was carried out at the following conditions: [Na<sub>3</sub>PO<sub>4</sub>] = [PP] = [3-TPP] = [4-TPP] = 50 mM, pH = 6, [Fe<sup>2+</sup>] = 1 mM. A negligible SMR removal rate (5% in Fig. 9a) in Na<sub>2</sub>SO<sub>4</sub> system was observed since the yields of ·OH generated in  $\text{Fe}^{2+}/\text{O}_2$  system via Haber-Weiss reactions (Eqs. 17 and 18 and Eq. 1) was below the detection limit by the fluorescent 2-hydroxyterephthalic acid (TAOH) in Fig. 9b when TA was used as the ·OH trapper to quantify ·OH. However, a higher SMR degradation was observed at the first 10 min with Na<sub>3</sub>PO<sub>4</sub> (14.00%), PP (14.87%), 3-TPP (39.00%) and 4-TPP (47.72%), respectively thanks to the formation of  $\text{Fe}^{2+}$ -ligand complexes, which could enhance ·OH formation in the  $\text{Fe}^{2+}/\text{O}_2$  system. Therefore, similar to  $\text{Fe}^{2+}$ -4-TPP complexes,  $\text{Fe}^{2+}$ -3-TPP,  $\text{Fe}^{2+}$ -PP and  $\text{Fe}^{2+}$ -PO<sub>4</sub> species might follow the mechanism of activating molecular oxygen to form ·OH via Eqs. 6–8 as reported in our previous works [26].

To confirm this assumption, photoluminescence method couple

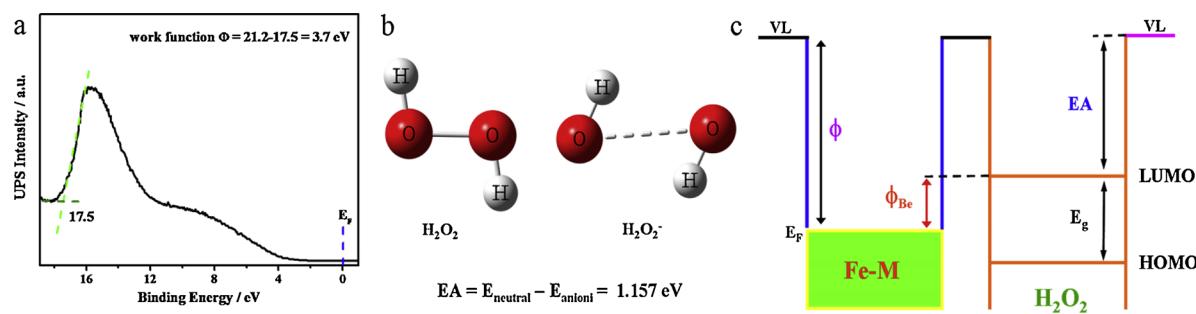


**Fig. 10.** UPS spectrum of  $\text{Fe}^{2+}$ -ligands (a), where He I radiation light excitation energy is approximately 21.2 eV. The electron affinity of the  $\text{H}_2\text{O}_2$ ,  $\text{H}_2\text{O}_2^-$  molecules calculated by DFT using B3LYP/6-311 + G(d) level (b). Energy level diagram of the  $\text{Fe}^{2+}$ -ligands and target molecule in contact and following the Schottky-Mott vacuum level alignment (c), in which VL,  $\Phi$ ,  $E_F$ ,  $\Phi_{\text{Be}}$ , EA, LUMO and HOMO stand for vacuum level, work function, Fermi level, electron injection barrier, energy gap, electron affinity, the lowest unoccupied and highest occupied molecular orbitals, respectively.

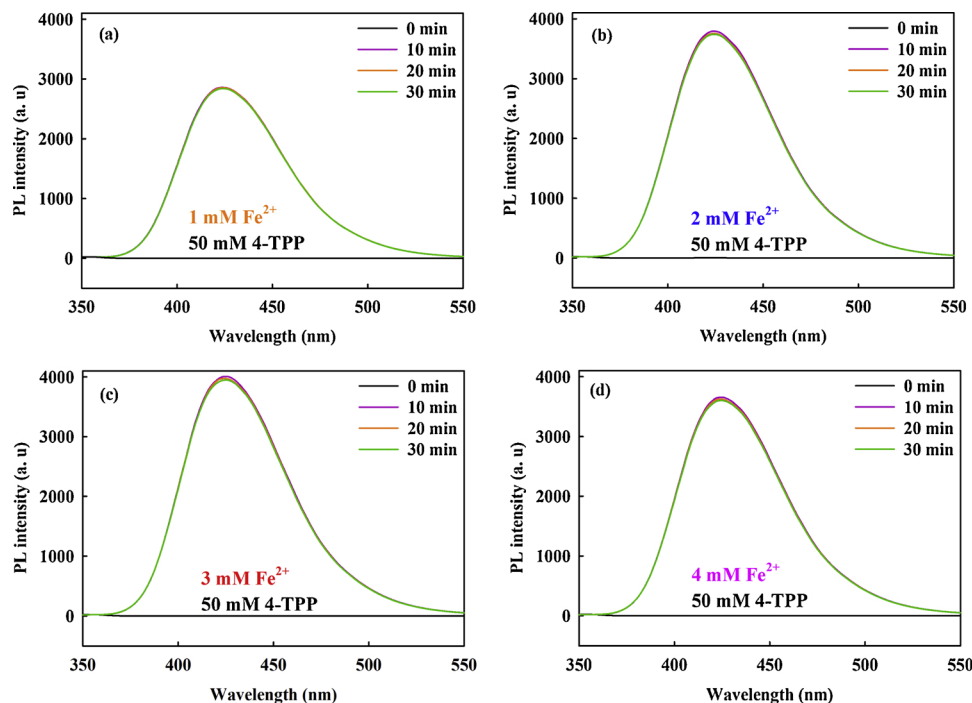


**Fig. 11.** PL spectra of TAOH for different  $\text{Fe}^{2+}$ -4-TPP concentrations. Conditions:  $\text{pH} = 6$ ,  $\text{Fe}^{2+} = 1\text{--}4\text{ mM}$ , air flow rate =  $500\text{ mL min}^{-1}$ ,  $[\text{TPP}] = 50\text{ mM}$ ,  $\text{pH} = 6$ .

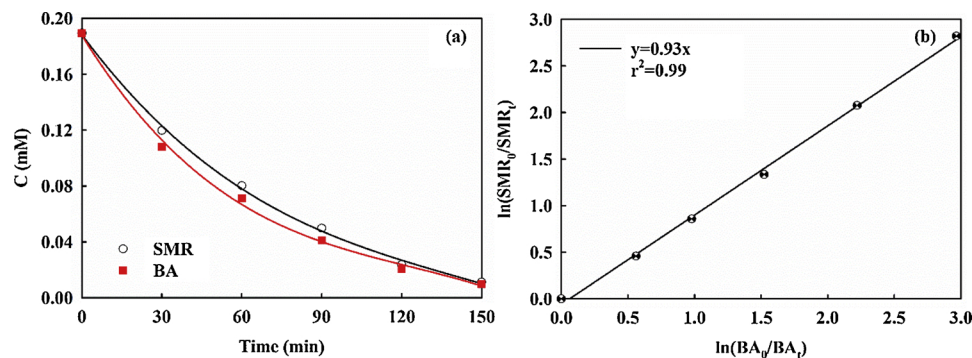


**Fig. 12.** Determination of the absolute rate constant of SMR oxidation by  $\cdot\text{OH}$  using the competition approach. Time course of SMR and BA concentration degraded by EF with the identical concentration of SMR and BA (0.189 mM) (a), Kinetic analysis of the data derived from a (b).

with ESR spectra was adopted to verify the dominant oxidizing species generated in the  $\text{Fe}^{2+}$ -ligands process. Expectedly, the formation of  $\cdot\text{OH}$  in  $\text{Fe}^{2+}\text{-4-TPP}$ ,  $\text{Fe}^{2+}\text{-3-TPP}$ ,  $\text{Fe}^{2+}\text{-PP}$ ,  $\text{Fe}^{2+}\text{-PO}_4$  systems was confirmed by the appearance of strong fluorescent TAOH peak (Fig. 9b) and the occurrence of strong characteristic signals of the DMPO- $\cdot\text{OH}$

adduct in the ESR spectra shown in Fig. 9c [55]. As deduced from Fig. 9, it could conclude that the order of  $\cdot\text{OH}$  generation ability among those compounds was given as follows:  $\text{Fe}^{2+}\text{-4-TPP} > \text{Fe}^{2+}\text{-3-TPP} > \text{Fe}^{2+}\text{-PP} \approx \text{Fe}^{2+}\text{-PO}_4$ , which was in good accordance with SMR degradation by  $\text{Fe}^{2+}$ -ligand complexes (Fig. 9a). Interestingly, SMR

**Table 2**

Aromatic intermediates and short-chain acids generated during SMR degradation by EF system.

No	Formula	Structure	[M + H] <sup>+</sup>	RT (min)	Analytical technique	m/z fragments
	C <sub>11</sub> H <sub>12</sub> N <sub>4</sub> O <sub>2</sub> S		265	0.22	LC-MS-MS	256.04, 06 (M <sup>+</sup> ), 156, 172, 110
A	C <sub>11</sub> H <sub>12</sub> N <sub>4</sub> O <sub>3</sub> S		281	1.69	LC-MS-MS	281(M <sup>+</sup> ), 253.79 (42%), 235.86 (40%)
B	C <sub>11</sub> H <sub>12</sub> N <sub>4</sub> O <sub>3</sub> S		281	1.69	LC-MS-MS	
C	C <sub>11</sub> H <sub>12</sub> N <sub>4</sub> O <sub>4</sub> S		291	2.25	LC-MS-MS	297 (M <sup>+</sup> ), 279, 217, 231, 110
D	C <sub>11</sub> H <sub>12</sub> N <sub>3</sub> O <sub>4</sub> S		282	0.25	LC-MS-MS	282 (M <sup>+</sup> ), 246, 241, 202
E	C <sub>11</sub> H <sub>12</sub> N <sub>4</sub> O <sub>5</sub> S		313	2.46	LC-MS-MS	313 (M <sup>+</sup> ), 304, 172, 263
F	C <sub>11</sub> H <sub>10</sub> N <sub>4</sub> O <sub>4</sub> S		295	1.58	LC-MS-MS	295 (M <sup>+</sup> ), 294, 215, 160, 247
G	C <sub>11</sub> H <sub>11</sub> N <sub>3</sub> O <sub>3</sub> S		266	1.01	LC-MS-MS	266(M <sup>+</sup> ), 248, 232, 222, 192, 130
H	C <sub>11</sub> H <sub>8</sub> N <sub>4</sub> O <sub>6</sub> S		325	1.559	LC-MS-MS	325 (M <sup>+</sup> ), 324, 306, 227, 223
I	C <sub>7</sub> H <sub>9</sub> N <sub>3</sub> O <sub>3</sub> S		216	1.92	LC-MS-MS	216 (M <sup>+</sup> ), 199, 181
J	C <sub>6</sub> H <sub>7</sub> NO <sub>3</sub> S		174	0.98	LC-MS-MS	174 (M <sup>+</sup> ), 159, 133, 128
K	C <sub>7</sub> H <sub>7</sub> N <sub>3</sub>		110	1.609	LC-MS-MS	110 (M <sup>+</sup> ), 93, 69
L	C <sub>6</sub> H <sub>5</sub> NO <sub>5</sub> S		204	1.95	LC-MS-MS	204(M <sup>+</sup> ), 187
M	C <sub>5</sub> H <sub>6</sub> N <sub>2</sub> O		111	2.01	LC-MS-MS	111(M <sup>+</sup> ), 96
N	C <sub>6</sub> H <sub>8</sub> N		94	0.71	LC-MS-MS	94(M <sup>+</sup> ), 80
O	C <sub>5</sub> H <sub>7</sub> N <sub>3</sub> O <sub>3</sub> S		189	1.52	LC-MS-MS	189(M <sup>+</sup> ), 161, 143, 130, 102, 58
P	C <sub>6</sub> NH <sub>7</sub> O		3.78		UPLC	
Q	C <sub>6</sub> H <sub>6</sub> O <sub>2</sub>		3.21		UPLC	
R	C <sub>4</sub> H <sub>4</sub> O <sub>4</sub>		2.20		UPLC	
S	CH <sub>2</sub> O <sub>2</sub>		1.31		UPLC	
T	C <sub>4</sub> H <sub>4</sub> O <sub>4</sub>		2.87		UPLC	
U	C <sub>2</sub> H <sub>2</sub> O <sub>4</sub>		0.95		UPLC	
V	CH <sub>3</sub> COOH		2.00		UPLC	

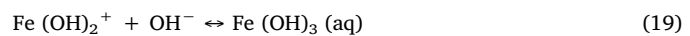
decay witnessed a steady state period after 10 min (Fig. 9a) due to a noncontinuous ·OH generation (Fig. SI. 5) caused by the lack of Fe<sup>2+</sup>-regeneration [26].

The electron injection barrier ( $\Phi_{Be}$ ) between the substrate materials and target molecules was further employed to gain insight of Fe<sup>2+</sup>-ligands complex for H<sub>2</sub>O<sub>2</sub> activation to form ·OH. As shown in Fig. 10a and Fig. SI. 6, with ultraviolet photoemission spectroscopy (UPS) technique, the work function ( $\Phi$ ) of Fe<sup>2+</sup>-4-TPP, Fe<sup>2+</sup>-3-TPP, Fe<sup>2+</sup>-PP and Fe<sup>2+</sup>-PO<sub>4</sub> were estimated to be about 1.2 eV, 1.0 eV, 2.8 eV, 3.7 eV, which is energy difference between the Fermi level (EF) and the vacuum level (VL) [56]. Then DFT calculation was used to obtain the energy level of optimized H<sub>2</sub>O<sub>2</sub>, H<sub>2</sub>O<sub>2</sub><sup>-</sup>, which is defined as electron affinity (EA)-an energy achieved by initially neutral molecule upon the introduction of an electron to the lowest unoccupied molecular orbital (LUMO) (Fig. 10b). It illustrated in Fig. 10c the electron injection barrier  $\Phi_{Be}$  could be deduced from  $\Phi_{Be} = \Phi - EA$  according to Schottky Mott rule, where  $\Phi_{Be}$  between Fe<sup>2+</sup>-4-TPP, Fe<sup>2+</sup>-3-TPP and H<sub>2</sub>O<sub>2</sub> was relatively lower compared to that of Fe<sup>2+</sup>-PP and Fe<sup>2+</sup>-PO<sub>4</sub>. This result confirmed the transfer of charge favoured between Fe<sup>2+</sup>-4-TPP, Fe<sup>2+</sup>-3-TPP and H<sub>2</sub>O<sub>2</sub>, which was in good agreement with PL and ESR results.

Therefore, different oxidation ability of Fe<sup>2+</sup>-ligands was responsible for SMR decay differences when various supporting electrolytes were used in the EF process (Fig. 8a). To go further, the total iron dissolved from Fe-F catalyst was monitored and results were given in Fig. 8c. A total Fe concentration of 1.67 mM, 2.00 mM, 3.08 mM, 4.06 mM 5.22 mM was found for Na<sub>2</sub>SO<sub>4</sub>, Na<sub>3</sub>PO<sub>4</sub>, PP, 3-TPP, 4-TPP, respectively. In addition, the final pH after electrolysis increased to 7.706 for Na<sub>2</sub>SO<sub>4</sub> electrolyte. However, pH was kept around the initial

pH 6 with 6.071, 6.051, 6.024, 6.07 for Na<sub>3</sub>PO<sub>4</sub>, PP, 3-TPP and 4-TPP, respectively, implying the buffer ability of polyphosphate-based electrolytes. Thus, the buffer ability guaranteed iron ions to keep dissolved through moving the balance to the left (Eq. 19) and then further promoting chemical corrosion of Fe-F catalyst (Eqs. 9 and 10), supporting by a higher total iron in Na<sub>3</sub>PO<sub>4</sub> (2 mM) than that in Na<sub>2</sub>SO<sub>4</sub> (1.67 mM) (Fig. 7c). The similar mechanism might take place for PP, 3-TPP and 4-TPP since a rise of total iron (3.08 mM, 4.06 mM, 5.22 mM) was observed, suggesting a relative higher buffer ability for 4-TPP, 3-TPP than that of PP, Na<sub>3</sub>PO<sub>4</sub>. Consequently, SMR decay in the 4-TPP supporting electrolyte was expected to be the highest because a higher iron released from Fe-F catalyst and the highest activity of Fe<sup>2+</sup>-4-TPP complex for ·OH generation. However, that was not the case in 4-TPP since ·OH generation was hindered by excessive Fe<sup>2+</sup> (Eq. 20) when it was more than 3 mM, revealing by the variance of ·OH intensity shown in Fig. 11. The ·OH intensity reflected by fluorescence in Fig. 9d was well explained a similar SMR degradation in 4-TPP and 3-TPP electrolytes.

In a word, SMR enhancement by polyphosphate-based electrolytes in EF was mainly associated with Fe<sup>2+</sup>-ligand compounds, which could activate oxygen to form additional ·OH. Among the five supporting electrolytes, 4-TPP and 3-TPP electrolytes have achieved higher SMR decays due to a relative higher activity for ·OH generation via Fe<sup>2+</sup>-4-TPP and Fe<sup>2+</sup>-3-TPP complexes.



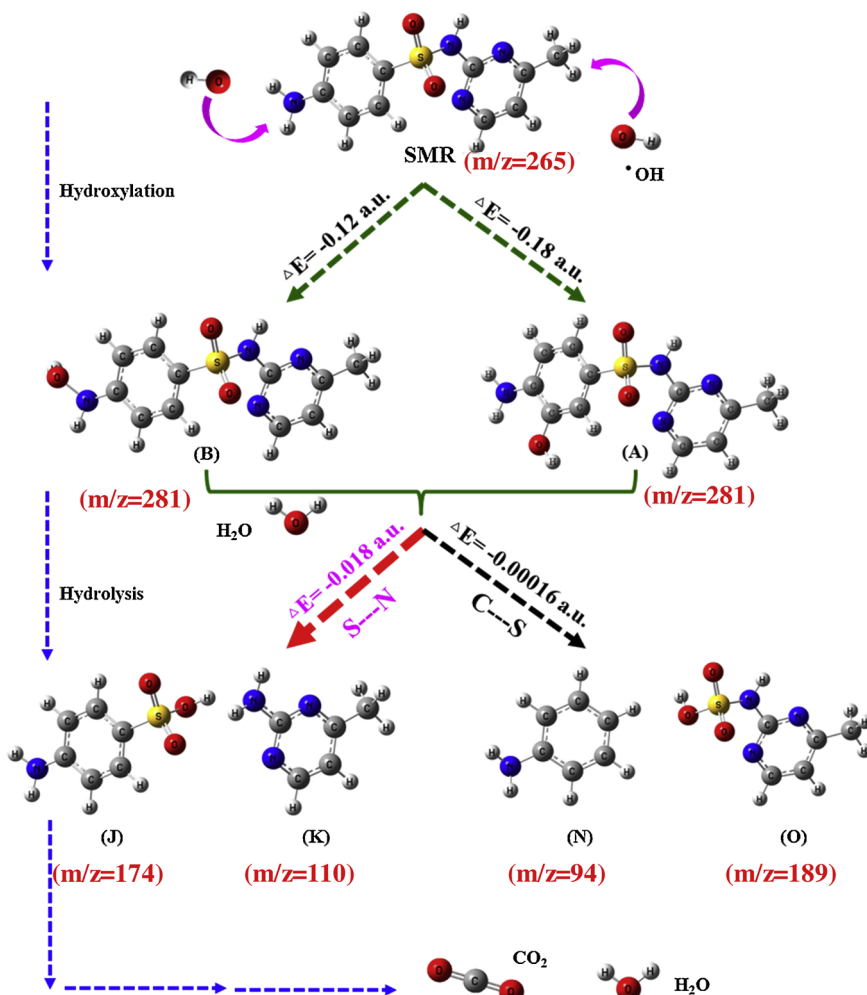


**Fig. 13.** A possible SMR degradation pathway deduced from theoretically calculation and detected by-products in EF process with B@Ni-F cathode and Fe-F catalyst.



### 3.5.2. SMR degradation kinetics

According to the above analysis, the dominant oxidizing species in the proposed EF process was ·OH. As a consequence, to assess the absolute (second order) rate constant for SMR ( $k_{abs(\text{SMR})}$ ) oxidation by ·OH, which has not been reported previously, competition kinetic method was applied using BA as a standard ·OH competitor with a well known absolute rate constant  $k_{abs(\text{BA})} = (5.91 \pm 0.54) \times 10^9 \text{ M}^{-1} \text{ s}^{-1}$  [33]. A solution containing the identical concentration (0.189 mM) of BA and SMR was degraded by the B@Ni-F/Fe-Foam electro-Fenton process. Calculated from Eq. 13,  $k_{abs(\text{SMR})}$  was determined to be  $(5.50 \pm 0.50) \times 10^9 \text{ M}^{-1} \text{ s}^{-1}$  (Fig. 12). Interestingly, this value was quite close to the analogous oxidation reaction of similar pharmaceuticals, like sulfamethazine ( $1.87 \times 10^9 \text{ M}^{-1} \text{ s}^{-1}$ ), sulfachloropyridazine ( $1.58 \times 10^9 \text{ M}^{-1} \text{ s}^{-1}$ ) [57,58].

### 3.5.3. Identification of aromatic intermediates and proposed SMR degradation pathway

To elucidate SMR degradation pathway in the EF with B@Ni-F cathode and Fe-F catalyst, UPLC-MS/MS coupled with UPLC, ionic chromatography was used to identify the intermediates. The detected byproducts were summarized in Table 2. Thus, a possible SMR degradation pathway by EF was proposed in Fig. SI. 7. According to previous investigations, hydroxylation of aniline residue of SMR, the cleavage of –S–N– and –C–S– were deemed as the dominant degradation pathways during sulfonamides oxidation when ·OH was involved

[59,60]. Regarding ·OH attack of aniline ring, a single and multiple hydroxylation of SMR were observed that came along with the formation of  $\text{C}_{11}\text{H}_{12}\text{N}_4\text{O}_3\text{S}$  (A,  $m/z = 281$ ),  $\text{C}_{11}\text{H}_{12}\text{N}_4\text{O}_3\text{S}$  (B,  $m/z = 281$ ),  $\text{C}_{11}\text{H}_{12}\text{N}_4\text{O}_4\text{S}$  (C,  $m/z = 297$ ),  $\text{C}_{11}\text{H}_{12}\text{N}_3\text{O}_4\text{S}$  (D,  $m/z = 282$ ),  $\text{C}_{11}\text{H}_{12}\text{N}_4\text{O}_5\text{S}$  (E,  $m/z = 313$ ), which was in accordance with previous research [61]. Then further oxidation or substitution of amino group generated F ( $\text{C}_{11}\text{H}_{10}\text{N}_4\text{O}_4\text{S}$ ,  $m/z = 295$ ) and 4-Hydroxy-N-(4-methyl-pyrimidin-2-yl)-benzenesulfonamide (G,  $\text{C}_{11}\text{H}_{11}\text{N}_3\text{O}_3\text{S}$ ,  $m/z = 266$ ). Consecutive oxidation of F produced H ( $\text{C}_{11}\text{H}_8\text{N}_4\text{O}_6\text{S}$ ,  $m/z = 325$ ), while  $\text{C}_7\text{H}_9\text{N}_3\text{O}_3\text{S}$  (I,  $m/z = 216$ ) was monitored by the cleavage of pyrimidine ring. In addition, hydroxyl radical attack on sulfonamide moiety would result in the breakage of S–N bond, forming 4-Amino-benzenesulfonic acid (J,  $m/z=174$ ) and the 4-Methyl-pyrimidin-2-ylamine (K,  $\text{C}_7\text{H}_7\text{N}_3$ ,  $m/z = 110$ ), while 4-Nitro-benzenesulfonic acid (L,  $\text{C}_6\text{H}_5\text{NO}_3\text{S}$ ,  $m/z = 174$ ) was produced via the oxidation of -NH<sub>2</sub> in K. Further oxidation of J yielded 4-Methyl-pyrimidin-2-ol (M,  $\text{C}_5\text{H}_6\text{N}_2\text{O}$ ,  $m/z = 111$ ) along with  $\text{NO}_3^-$  release. Another possible decomposition way was related to the cleavage of S–C bond, where aniline (N,  $\text{C}_6\text{H}_8\text{N}$ ,  $m/z = 94$ ) and (4-Methyl-pyrimidin-2-yl)-sulfamic acid (O,  $\text{C}_5\text{H}_6\text{N}_3\text{O}_3\text{S}$ ,  $m/z = 189$ ) were detected during SMR degradation. Aniline was experienced further oxidation to form 4-Amino-phenol (P), hydroquinone (Q) and benzoquinone and it was in good agreement with the appearance of yellowish color. Breakage of benzenic ring of aromatic derivatives would form carboxylic acids (formic acid, maleic acid, oxalic acid, acetic acid and fumaric acid) along with the release of  $\text{NH}_4^+$ ,  $\text{NO}_3^-$ ,  $\text{SO}_4^{2-}$  and TOC removal [62], which would discuss in the following section.

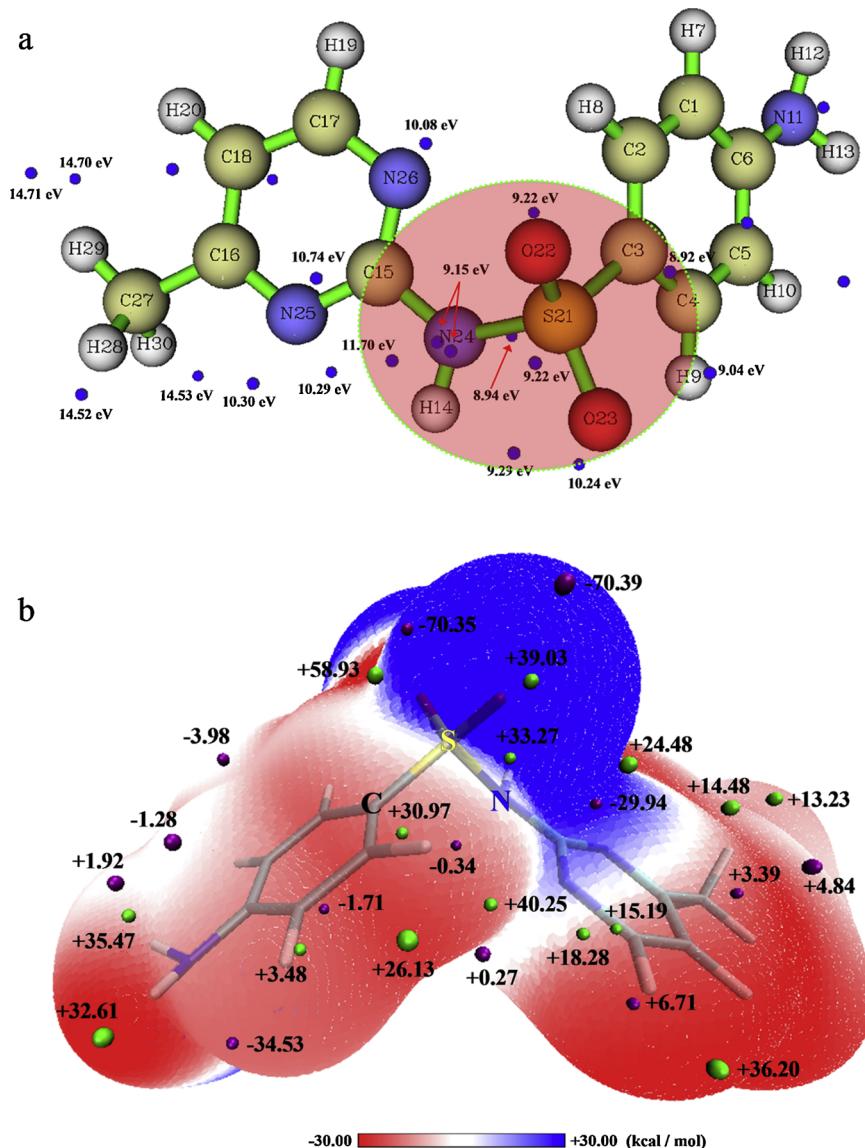


**Fig. 14.** (a) ALIE analysis and (b) 3D ESP mapping on SMR molecular vdW surface. In ALIE analysis, the blue points denote the surface minima, and the energy values denote the ALIE on the corresponding positions. The unit is eV. In 3D ESP mapping, the red areas meant local negatively charged areas, otherwise it represented positively charged areas. And the green points denote the surface maxima and the purple points represent the surface minima. The corresponding values around the green and purple points are the local charge values. The unit is kcal/mol. (For interpretation of the references to colour in this figure legend, the reader is referred to the web version of this article).

Furthermore, first-principles calculations along with thermodynamic analysis were employed to predict the energetically feasible option among the above-mentioned three mechanisms including hydroxylation of aniline residue, the cleavage of  $-S-N-$  and  $-C-S-$  bonds. Energetics was monitored by estimating the total energy variance ( $\Delta E$ ) of all substances before and after reaction that might occur. In general, a reaction releases more heat (energy) suggests the trend for a thermodynamic facility [63]. The optimized structures, their corresponding energies and energy changes of possible reaction paths show in Fig. SI. 8-9. It was found that thermodynamic facility falls in following order: hydroxylation of SMR ( $\Delta E = 0.12/0.18$  a.u.)  $>$   $-S-N-$  ( $\Delta E = 0.018$  a.u.)  $>$   $-C-S-$  ( $\Delta E = 0.00016$  a.u.), indicating the hydroxylation of aniline residue of SMR facilitated the SMR degradation pathway, followed with the breakage of  $-S-N-$  bond, as shown in Fig. 13. Because the energy change for the cleavage of  $-S-N-$  bond was 100-fold than that of the cleavage of  $-C-S-$  ( $\Delta E = 0.00016$  a.u.). Therefore, the plausible degradation pathway of SMR in Fig. 13 was proposed by combining the detected by-products from UPLC-MS/MS and the first-principles calculations, where the hydroxylation of aniline residue of SMR was dominant, and the cleavage of  $-S-N-$  was subsequently occurred. Furthermore, DFT calculation, specifically ALIE analysis (Fig. 14a) and 3D ESP (Fig. 14b) mapping were adopted to assess its nucleophilic and electrophilic sites on SMR molecular. On

vdW surface of a molecular, the electrophilic and free radical reactions are generally prone to occur at the site with the lowest ALIE value, due to the weaker electron binding ability or the stronger electron activity around the lowest ALIE position. As shown in Fig. 14a, the area around the S-N bond displays several ALIE minima points, such as, 8.94, 9.15, 9.15, 9.22 and 9.29 eV. But only a minima point is observed around the S-C bond. Hence, this result indicated that the electrophilic reaction or free radical reaction is more likely to occur near the S-C site. Meanwhile, it is easy to see from the 3D ESP mapping that the area of S-N bond places a partial positive charge region or neutral area, and the area of S-C bond obviously positions partial negative charge region. Moreover, there are some surface maxima values around the S-N bond, such as, 39.03, 33.27 and 24.48 kcal/mol. These results demonstrated that the most possibility regions to electrophilic or to free radical attacked is the site around S-N bond. Therefore, we can conclude that in comparison to  $-C-S-$  bond, the  $-S-N-$  bond was more likely to be attacked by free radical, as confirmed by ALIE analysis and 3D ESP mapping, and it is in accordance with the above-mentioned SMR degradation pathway.

### 3.5.4. Time-course of mineralization, inorganic ions, carboxylic acids and toxicity assessment during SMR degradation

Fig. 15a illustrates the time course of the TOC/TN variance of SMR

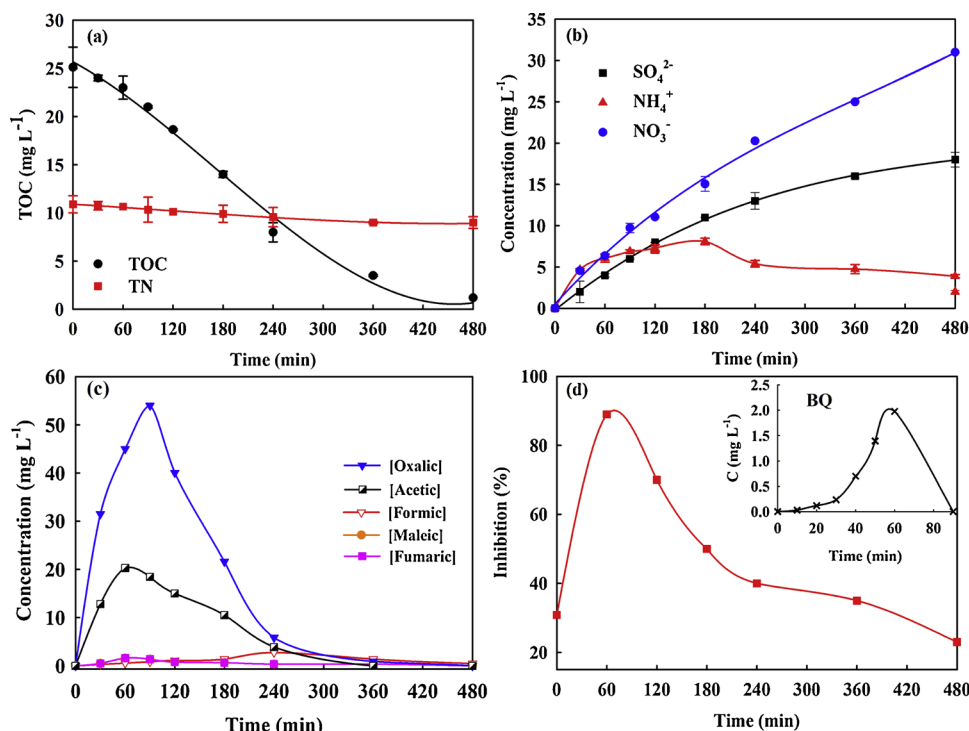


Fig. 15. Evaluation of total organic carbon (TOC), total nitrogen (TN) (a), concentration of  $\text{NH}_4^+$ ,  $\text{SO}_4^{2-}$ ,  $\text{NO}_3^-$  (b), short-chain carboxylic acids (c), evolution of toxicity (d) during SMR degradation by EF with B@Ni-F cathode and Fe-F catalyst.

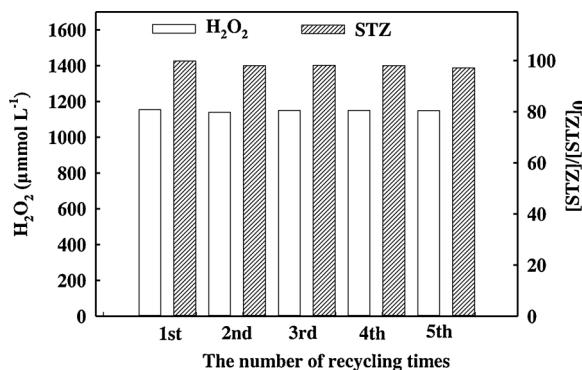


Fig. 16. The long-term stability of B@Ni-F cathode regarding  $\text{H}_2\text{O}_2$  generation and STZ degradation.

degradation, where TOC removal rate could reach 95.22% after 8 h, meaning good mineralization was achieved. In addition, the transformation of the initial N, S into  $\text{NO}_3^-$ ,  $\text{NH}_4^+$ ,  $\text{SO}_4^{2-}$  was investigated and results were shown in Fig. 15b. The mineralization started at the beginning of the treatment since the formation of these inorganic ions were observed as electrolysis begun. The concentration of  $\text{NO}_3^-$  and  $\text{NH}_4^+$  accumulated at  $31.00 \text{ mg L}^{-1}$ ,  $3.88 \text{ mg L}^{-1}$  after 8 h treatment, accounting for 64.27% and 14.14% of the initial N. The total nitrogen remained in the solution decreased to  $0.64 \text{ mM}$ , implying 13.5% TN has been lost in the form of volatile  $\text{N}_x\text{O}_y$  compounds as previously investigated by Ridruejo [64].

Aside from the evolution of inorganic ions, aliphatic carboxylic acid (the final byproducts before mineralization) was depicted in Fig. 15c. Acetic acid ( $20.4 \text{ mg L}^{-1}$ ) and oxalic acid ( $45.02 \text{ mg L}^{-1}$ ) reached their maximum concentrations at 60 min. Fumaric and maleic acid were formed and progressively degraded, yielding mainly oxalic acid. Formic acid reached its highest level ( $2.76 \text{ mg L}^{-1}$ ) after 6 h and then it was mineralized into  $\text{CO}_2$ .

Considering the fact that more toxic byproducts than the initial

organic pollutant would form during AOPs treatment, it was worthwhile stressing the evolution of the toxicity of SMR degraded by EF [65]. Therefore, toxicity evolution of SMR ( $50 \text{ mg L}^{-1}$ ) over 6 h electrolysis was monitored according to the measurement of bioluminescence inhibition of the marine *V. fischeri* bacteria (Microtox) brought about SMR and/or its intermediates. As can be seen in Fig. 15d, it was characterized by an initial increase of bioluminescence inhibition (from 30.82% to 89%) at the first 60 min electrolysis, indicating more toxic cyclic byproducts were generated in the first stage of EF treatment since there compounds were predominant during this period. It was interesting to note that the time course of *p*-benzoquinone (BQ) concentration (insert in Fig. 15d) was close to toxicity evolution, suggesting BQ was, at least partly, responsible for the augment toxicity during the first stage of EF. It was in good agreement with Dirany's investigations that BQ was accounted for the rising toxicity during sulfachloropyridazine/sulfamethoxazole degradation by EF [65,66]. The toxicity after 1 h decayed and reached its minimum inhibition value (20%) in the final stage of electrolysis, explaining by the formation of low toxic aliphatic carboxylic acids generated from the destruction of the cyclic byproducts and BQ [66]. In a word, it provides evidence that EF with B@Ni-F cathode and Fe-F catalyst is a promising process for the sulfonamide antibiotics remediation regarding its complete removal, mineralization coupled with the total detoxification.

Moreover, the long-term stability of the newly fabricated B@Ni-F cathode was confirmed using the same cathode for five runs in Fig. 16, where both the final  $\text{H}_2\text{O}_2$  accumulation and STZ degradation ranged within an acceptable error.

#### 4. Conclusions

A novel B@Ni-F cathode derived from renewable biomass along with Fe-F catalyst was used in EF for SMR degradation.  $\text{H}_2\text{O}_2$  generation ability on B@Ni-F improved 14 times compared with raw Ni-F cathode due to an improvement of hydrophilicity, active surface area coupled with charge transfer resistance dropped from  $95.7 \Omega$  to  $7.18 \Omega$ . Regarding SMR degradation, 4-TPP and 3-TPP electrolytes have relative

higher  $k_{app}$  with  $2.73 \times 10^{-2} \text{ min}^{-1}$  and  $2.70 \times 10^{-2} \text{ min}^{-1}$ , respectively thanks to a higher buffer ability and its consequence for a high iron accumulated in the bulk from Fe-F catalyst. The absolute rate constant for oxidation of SMR by ·OH was determined to be  $(3.4 \pm 0.09) \times 10^9 \text{ M}^{-1} \text{ s}^{-1}$ . A plausible reaction pathway was proposed for SMR degradation/mineralization during B@Ni-F/Fe-F EF process, where the hydroxylation of aniline residue of SMR was dominant, and the cleavage of –S–N– subsequently was occurred according to the by-products detected by UPLC-MS/MS and DFT calculations.

## Acknowledgements

The work was supported by the National Key Research and Development Plan of China (No. 2016YFC0401102) and Postgraduate Education Reform Project of Harbin Institute of Technology (No. JGYJ-2018030). We appreciate Dr. Zheyu Li for precious discussions and technical support. The authors thank Dr. Arramel from Department of Physics, National University of Singapore, 2 Science Drive 3, 117542, Singapore for UPS test.

## Appendix A. Supplementary data

Supplementary material related to this article can be found, in the online version, at doi:<https://doi.org/10.1016/j.apcatb.2019.117796>.

## References

- [1] X. Liu, Y. Zhou, J. Zhang, L. Luo, Y. Yang, H. Huang, H. Peng, L. Tang, Y. Mu, Insight into electro-Fenton and photo-Fenton for the degradation of antibiotics: mechanism study and research gaps, *Chem. Eng. J.* 347 (2018) 379–397, <https://doi.org/10.1016/j.cej.2018.04.142>.
- [2] T. Zhang, B. Li, Occurrence, transformation, and fate of antibiotics in municipal wastewater treatment plants, *Crit. Rev. Environ. Sci. Technol.* 41 (2011) 951–998, <https://doi.org/10.1080/10643380903392692>.
- [3] N. Liu, W. Huang, Z. Li, H. Shao, M. Wu, J. Lei, L. Tang, Radiolytic decomposition of sulfonamide antibiotics: implications to the kinetics, mechanisms and toxicity, *Sep. Sci. Technol.* 202 (2018) 259–265, <https://doi.org/10.1016/j.seppur.2018.03.060>.
- [4] J. Casado, Towards industrial implementation of Electro-Fenton and derived technologies for wastewater treatment: a review, *J. Environ. Chem. Eng.* 7 (2019) 102823–102838, <https://doi.org/10.1016/j.jece.2018.102823>.
- [5] E. Brillas, I. Sirés, M.A. Oturan, Electro-Fenton process and related electrochemical technologies based on Fenton's reaction chemistry, *Chem. Rev.* 109 (2009) 6570–6631, <https://doi.org/10.1021/cr900136g>.
- [6] I. Sirés, E. Brillas, M.A. Oturan, M.A. Rodrigo, M. Panizza, Electrochemical advanced oxidation processes: today and tomorrow. A review, *Environ. Sci. Pollut. Res.* 21 (2014) 8336–8367, <https://doi.org/10.1007/s11356-014-2783-1>.
- [7] I. Sirés, E. Brillas, M. Zhou, M.A. Oturan, I. Sirés (Eds.), *Electro-Fenton Process: Fundamentals and Reactivity*, Springer Singapore, Singapore, 2018, pp. 1–28.
- [8] Y. Wang, W. Jiang, W. Luo, X. Chen, Y. Zhu, Ultrathin nanosheets g-C<sub>3</sub>N<sub>4</sub>@Bi<sub>2</sub>WO<sub>6</sub> core-shell structure via low temperature reassembled strategy to promote photocatalytic activity, *Appl. Catal. B: Environ.* 237 (2018) 633–640, <https://doi.org/10.1016/j.apcatb.2018.06.013>.
- [9] E. Bocos, O. Iglesias, M. Pazos, M. Ángeles Sanromán, Nickel foam a suitable alternative to increase the generation of Fenton's reagents, *Process Saf. Environ. Prot.* 101 (2016) 34–44, <https://doi.org/10.1016/j.psep.2015.04.011>.
- [10] O. Iglesias, J. Mejide, E. Bocos, M.Á. Sanromán, M. Pazos, New approaches on heterogeneous electro-Fenton treatment of winery wastewater, *Electrochim. Acta* 169 (2015) 134–141, <https://doi.org/10.1016/j.electacta.2015.04.062>.
- [11] J. Qin, Q. Chen, C. Yang, Y. Huang, Research process on property and application of metal porous materials, *J. Alloys Compd.* 654 (2016) 39–44, <https://doi.org/10.1016/j.jallcom.2015.09.148>.
- [12] A.L. Cazetta, L. Spessato, K.C. Bedin, I.P.F.A. Souza, R.A. Araújo, A.F. Martins, T.L. Silva, R. Silva, V.C. Almeida, Metal-free ovalbumin-derived N-S-co-doped nanoporous carbon materials as efficient electrocatalysts for oxygen reduction reaction, *Appl. Surf. Sci.* 467–468 (2019) 75–83, <https://doi.org/10.1016/j.apsusc.2018.10.140>.
- [13] Q. Tang, D. Wang, D.M. Yao, C.W. Yang, Y.C. Sun, Highly efficient electro-generation of hydrogen peroxide using NCNT/NF/CNT air diffusion electrode for electro-Fenton degradation of p-nitrophenol, *Water Sci. Technol.* 73 (2015) 1652–1658, <https://doi.org/10.2166/wst.2015.647>.
- [14] F. Deng, S. Qiu, H. Olvera-vargas, Y. Zhu, W. Gao, J. Yang, F. Ma, Electrocatalytic sulfathiazole degradation by a novel nickel-foam cathode coated with nitrogen-doped porous carbon, *Electrochim. Acta* 297 (2019) 21–30, <https://doi.org/10.1016/j.electacta.2018.11.180>.
- [15] J. Liang, D. Tang, L. Huang, Y. Chen, W. Ren, J. Sun, High oxygen reduction reaction performance nitrogen-doped biochar cathode: a strategy for comprehensive utilizing nitrogen and carbon in water hyacinth, *Bioresour. Technol.* 267 (2018) 524–531, <https://doi.org/10.1016/j.biotech.2018.07.085>.
- [16] S. Zhu, X. Huang, F. Ma, L. Wang, X. Duan, S. Wang, Catalytic removal of aqueous contaminants on N-doped graphitic biochars: inherent roles of adsorption and nonradical mechanisms, *Environ. Sci. Technol.* 52 (2018) 8649–8658, <https://doi.org/10.1021/acs.est.8b01817>.
- [17] H. Zhu, X. Wang, F. Yang, X. Yang, Promising carbons for supercapacitors derived from fungi, *Adv. Mater.* 23 (2011) 2745–2748, <https://doi.org/10.1002/adma.201100901>.
- [18] S. Gao, M. Wang, Y. Chen, M. Tian, Y. Zhu, X. Wei, T. Jiang, An advanced electro-Fenton degradation system with triboelectric nanogenerator as electric supply and biomass-derived carbon materials as cathode catalyst, *Nano Energy* 45 (2018) 21–27, <https://doi.org/10.1016/j.nanoen.2017.12.021>.
- [19] S. Ye, G. Zeng, H. Wu, C. Zhang, J. Liang, J. Dai, Z. Liu, W. Xiong, J. Wan, P. Xu, M. Cheng, Co-occurrence and interactions of pollutants, and their impacts on soil remediation—a review, *Crit. Rev. Env. Sci. Technol.* 47 (2017) 1528–1553, <https://doi.org/10.1080/10643389.2017.1386951>.
- [20] S. Ye, G. Zeng, H. Wu, J. Liang, C. Zhang, J. Dai, W. Xiong, B. Song, S. Wu, J. Yu, The effects of activated biochar addition on remediation efficiency of co-composting with contaminated wetland soil, *Resour. Conserv. Recycl.* 140 (2019) 278–285, <https://doi.org/10.1016/j.resconrec.2018.10.004>.
- [21] S. Ye, M. Yan, X. Tan, J. Liang, G. Zeng, H. Wu, B. Song, C. Zhou, Y. Yang, H. Wang, Facile assembled biochar-based nanocomposite with improved graphitization for efficient photocatalytic activity driven by visible light, *Appl. Catal. B* 250 (2019) 78–88, <https://doi.org/10.1016/j.apcatb.2019.03.004>.
- [22] S. Ye, G. Zeng, H. Wu, C. Zhang, J. Dai, J. Liang, J. Yu, X. Ren, H. Yi, M. Cheng, C. Zhang, Biological technologies for the remediation of co-contaminated soil, *Crit. Rev. Biotechnol.* 37 (2017) 1062–1076, <https://doi.org/10.1080/07388551.2017.1304357>.
- [23] K.G. Roberts, B.A. Gloy, S. Joseph, N.R. Scott, J. Lehmann, Life cycle assessment of biochar systems: estimating the energetic, economic, and climate change potential, *Environ. Sci. Technol.* 44 (2010) 827–833, <https://doi.org/10.1021/es902266r>.
- [24] H. Zheng, Z. Wang, X. Deng, J. Zhao, Y. Luo, J. Novak, S. Herbert, B. Xing, Characteristics and nutrient values of biochars produced from giant reed at different temperatures, *Bioresour. Technol.* 130 (2013) 463–471, <https://doi.org/10.1016/j.biotech.2012.12.044>.
- [25] L. Wang, M. Cao, Z. Ai, L. Zhang, Dramatically enhanced aerobic atrazine degradation with Fe@Fe<sub>2</sub>O<sub>3</sub> core-shell nanowires by tetrapolyphosphate, *Environ. Sci. Technol.* 48 (2014) 3354–3362, <https://doi.org/10.1021/es404741x>.
- [26] F. Deng, O. Garcia-Rodriguez, H. Olvera-Vargas, S. Qiu, O. Lefebvre, J. Yang, Iron-foam as a heterogeneous catalyst in the presence of tripolyphosphate electrolyte for improving electro-Fenton oxidation capability, *Electrochim. Acta* 272 (2018) 176–183, <https://doi.org/10.1016/j.electacta.2018.03.160>.
- [27] E.M. Siedlecka, A. Ofiarska, A.F. Borzyszkowska, A. Bialk-Bielinska, P. Stepnowski, A. Pieczyńska, Cytostatic drug removal using electrochemical oxidation with BDD electrode: degradation pathway and toxicity, *Water Res.* 144 (2018) 235–245, <https://doi.org/10.1016/j.watres.2018.07.035>.
- [28] X. Yang, E.E. Kwon, X. Dou, M. Zhang, K. Kim, D.C.W. Tsang, Y.S. Ok, Fabrication of spherical biochar by a two-step thermal process from waste potato peel, *Sci. Total Environ.* 626 (2018) 478–485, <https://doi.org/10.1016/j.scitotenv.2018.01.052>.
- [29] C. Zhang, Y. Dai, H. Chen, Y. Ma, B. Jing, Z. Cai, Y. Duan, B. Tang, J. Zou, Carbon-thin-layer protected WP with no passivation supported on acid-treated expanded graphite as efficient Pt co-catalysts for methanol oxidation and oxygen reduction reactions, *J. Mater. Chem. A* 6 (2018) 22636–22644, <https://doi.org/10.1039/C8TA0285E>.
- [30] O. Garcia-Rodriguez, Y.Y. Lee, H. Olvera-Vargas, F. Deng, Z. Wang, O. Lefebvre, Mineralization of electronic wastewater by electro-Fenton with an enhanced graphene-based gas diffusion cathode, *Electrochim. Acta* 276 (2018) 12–20, <https://doi.org/10.1016/j.electacta.2018.04.076>.
- [31] R. Yin, W. Guo, H. Wang, J. Du, X. Zhou, Q. Wu, H. Zheng, J. Chang, N. Ren, Selective degradation of sulfonamide antibiotics by peroxymonosulfate alone: direct oxidation and nonradical mechanisms, *Chem. Eng. J.* 334 (2018) 2539–2546, <https://doi.org/10.1016/j.cej.2017.11.174>.
- [32] E. Jimenez-Relinque, M. Castellote, Hydroxyl radical and free and shallowly trapped electron generation and electron/hole recombination rates in TiO<sub>2</sub> photocatalysis using different combinations of anatase and rutile, *Appl. Catal. A Gen.* 565 (2018) 20–25, <https://doi.org/10.1016/j.apcata.2018.07.045>.
- [33] C.R. Keenan, D.L. Sedlak, Ligand-enhanced reactive oxidant generation by nanoparticulate zero-valent iron and oxygen, *Environ. Sci. Technol.* 42 (2008) 6936–6941, <https://doi.org/10.1021/es081438f>.
- [34] B. Chen, Z. Chao, H. He, C. Huang, Y. Liu, W. Yi, X. Wei, J. An, Towards a full understanding of the nature of Ni(II) species and hydroxyl groups over highly siliceous HZSM-5 zeolite supported nickel catalysts prepared by a deposition-precipitation method, *Dalton Trans.* 45 (2016) 2720–2739, <https://doi.org/10.1039/C4DT00399C>.
- [35] M.F. El-Banna, A. Mosa, B. Gao, X. Yin, Z. Ahmad, H. Wang, Sorption of lead ions onto oxidized bagasse-biochar mitigates Pb-induced oxidative stress on hydroponically grown chicory: experimental observations and mechanisms, *Chemosphere* 208 (2018) 887–898, <https://doi.org/10.1016/j.chemosphere.2018.06.052>.
- [36] T. Zhao, Y. Yao, D. Li, F. Wu, C. Zhang, B. Gao, Facile low-temperature one-step synthesis of pomelo peel biochar under air atmosphere and its adsorption behaviors for Ag(I) and Pb(II), *Sci. Total Environ.* 640–641 (2018) 73–79, <https://doi.org/10.1016/j.scitotenv.2018.05.251>.
- [37] A. Bartyzel, Effect of molar ratios of reagents and solvent on the complexation process of nickel(II) ions by the N<sub>2</sub>O<sub>3</sub>-donor Schiff base, *Polyhedron* 134 (2017) 30–40, <https://doi.org/10.1016/j.poly.2017.06.004>.
- [38] S. Rezgui, A. Amrane, F. Fourcade, A. Assadi, L. Monser, N. Adhoum, Electro-Fenton

- catalyzed with magnetic chitosan beads for the removal of Chlordimeform insecticide, *Appl. Catal. B: Environ.* 226 (2018) 346–359, <https://doi.org/10.1016/j.apcatb.2017.12.061>.
- [39] Z. Lu, G. Chen, S. Siahrostami, Z. Chen, K. Liu, J. Xie, L. Liao, T. Wu, D. Lin, Y. Liu, T.F. Jaramillo, J.K. Nørskov, Y. Cui, High-efficiency oxygen reduction to hydrogen peroxide catalysed by oxidized carbon materials, *Nat. Catal.* 1 (2018) 156–162, <https://doi.org/10.1038/s41929-017-0017-x>.
- [40] M.M. Mian, G. Liu, B. Yousaf, B. Fu, H. Ullah, M.U. Ali, Q. Abbas, M.A. Mujtaba Munir, L. Ruijia, Simultaneous functionalization and magnetization of biochar via NH<sub>3</sub> ambience pyrolysis for efficient removal of Cr (VI), *Chemosphere* 208 (2018) 712–721, <https://doi.org/10.1016/j.chemosphere.2018.06.021>.
- [41] Q. Hao, R. Wang, H. Lu, C.A. Xie, W. Ao, D. Chen, C. Ma, W. Yao, Y. Zhu, One-pot synthesis of C/Bi<sub>x</sub>Bi<sub>2</sub>O<sub>3</sub> composite with enhanced photocatalytic activity, *Appl. Catal. B: Environ.* 219 (2017) 63–72, <https://doi.org/10.1016/j.apcatb.2017.07.030>.
- [42] Y. Zhu, S. Qiu, F. Ma, G. Li, F. Deng, Y. Zheng, Melamine-derived carbon electrode for efficient H<sub>2</sub>O<sub>2</sub> electro-generation, *Electrochim. Acta* 261 (2018) 375–383, <https://doi.org/10.1016/j.electacta.2017.12.122>.
- [43] D. Guo, R. Shibuya, C. Akiba, S. Saji, T. Kondo, J. Nakamura, Active sites of nitrogen-doped carbon materials for oxygen reduction reaction clarified using model catalysts, *Science* 351 (2016) 361–365, <https://doi.org/10.1126/science.aad0832>.
- [44] F. Deng, H. Olvera-Vargas, O. Garcia-Rodriguez, S. Qiu, J. Yang, O. Lefebvre, The synergistic effect of nickel-iron-foam and tripolyphosphate for enhancing the electro-Fenton process at circum-neutral pH, *Chemosphere* 201 (2018) 687–696, <https://doi.org/10.1016/j.chemosphere.2018.02.186>.
- [45] M.T. Moreira, I. Noya, G. Feijoo, The prospective use of biochar as adsorption matrix—a review from a lifecycle perspective, *Bioresour. Technol.* 246 (2017) 135–141, <https://doi.org/10.1016/j.biortech.2017.08.041>.
- [46] W. Yang, M. Zhou, J. Cai, L. Liang, G. Ren, L. Jiang, Ultrahigh yield of hydrogen peroxide on graphite felt cathode modified with electrochemically exfoliated graphene, *J. Mater. Chem. A* 5 (2017) 8070–8080, <https://doi.org/10.1039/C7TA01534H>.
- [47] X. Song, H. Ren, J. Ding, C. Wang, X. Yin, H. Wang, One-step nanocasting synthesis of sulfur and nitrogen co-doped ordered mesoporous carbons as efficient electrocatalysts for oxygen reduction, *Mater. Lett.* 159 (2015) 280–283, <https://doi.org/10.1016/j.matlet.2015.06.112>.
- [48] F. Deng, H. Olveravargas, O. Garciarodriguez, S. Qiu, J. Yang, O. Lefebvre, The synergistic effect of nickel-iron-foam and tripolyphosphate for enhancing the electro-Fenton process at circum-neutral pH, *Chemosphere* 201 (2018) 687–696, <https://doi.org/10.1016/j.chemosphere.2018.02.186>.
- [49] B. Li, C. Zhao, J. Liu, Q. Zhang, Electrosynthesis of hydrogen peroxide synergistically catalyzed by atomic Co-N<sub>x</sub>-C sites and oxygen functional groups in noble-metal-free electrocatalysts, *Adv. Mater.* 0 (2019) 1808173, , <https://doi.org/10.1002/adma.201808173>.
- [50] O. Garcia-Rodriguez, Y.L. Yi, H. Olvera-Vargas, F. Deng, Z. Wang, O. Lefebvre, Mineralization of electronic wastewater by electro-Fenton with an enhanced graphene-based gas diffusion cathode, *Electrochim. Acta* 276 (2018) 12–20, <https://doi.org/10.1016/j.electacta.2018.04.076>.
- [51] G. Coria, I. Sirés, E. Brillas, J.L. Nava, Influence of the anode material on the degradation of naproxen by Fenton-based electrochemical processes, *Chem. Eng. J.* 304 (2016) 817–825, <https://doi.org/10.1016/j.cej.2016.07.012>.
- [52] Z. Pan, K. Wang, Y. Wang, P. Tsikararas, S. Song, In-situ electrosynthesis of hydrogen peroxide and wastewater treatment application: a novel strategy for graphite felt activation, *Appl. Catal. B: Environ.* 237 (2018) 392–400, <https://doi.org/10.1016/j.apcatb.2018.05.079>.
- [53] J. Teng, J. Zhang, X. Wang, S. You, Chlorophenolic compounds degradation based on electrolyte-free electrochemical cells, *ACS Sustain. Chem. Eng.* 6 (2018) 4516–4520, <https://doi.org/10.1021/acssuschemeng.8b00720>.
- [54] Y. Mu, Z. Ai, L. Zhang, Phosphate shifted oxygen reduction pathway on Fe@Fe<sub>2</sub>O<sub>3</sub> core-shell nanowires for enhanced reactive oxygen species generation and aerobic 4-chlorophenol degradation, *Environ. Sci. Technol.* 51 (2017) 8101–8109, <https://doi.org/10.1021/acs.est.7b01896>.
- [55] W. Yang, Y. Zhu, F. You, L. Yan, Y. Ma, C. Lu, P. Gao, Q. Hao, W. Li, Insights into the surface-defect dependence of molecular oxygen activation over birnessite-type MnO<sub>2</sub>, *Appl. Catal. B: Environ.* 233 (2018) 184–193, <https://doi.org/10.1016/j.apcatb.2018.03.107>.
- [56] J. Zou, S. Wu, Y. Liu, Y. Sun, Y. Cao, J. Hsu, A.T. Shen Wee, J. Jiang, An ultra-sensitive electrochemical sensor based on 2D g-C<sub>3</sub>N<sub>4</sub>/CuO nanocomposites for dopamine detection, *Carbon* 130 (2018) 652–663, <https://doi.org/10.1016/j.carbon.2018.01.008>.
- [57] N. Oturan, C.T. Aravindakumar, H. Olvera-Vargas, M.M. Sunil Paul, M.A. Oturan, Electro-Fenton oxidation of para-aminosalicylic acid: degradation kinetics and mineralization pathway using Pt/carbon-felt and BDD/carbon-felt cells, *Environ. Sci. Pollut. Res.* 25 (2018) 20363–20373, <https://doi.org/10.1007/s11356-017-9309-6>.
- [58] N. Barhoumi, H. Olvera-Vargas, N. Oturan, D. Huguenot, A. Gadri, S. Ammar, E. Brillas, M.A. Oturan, Kinetics of oxidative degradation/mineralization pathways of the antibiotic tetracycline by the novel heterogeneous electro-Fenton process with solid catalyst chalcopyrite, *Appl. Catal. B: Environ.* 209 (2017) 637–647, <https://doi.org/10.1016/j.apcatb.2017.03.034>.
- [59] H. Yang, S. Zhuang, Q. Hu, L. Hu, L. Yang, C. Au, B. Yi, Competitive reactions of hydroxyl and sulfate radicals with sulfonamides in Fe<sup>2+</sup>/S<sub>2</sub>O<sub>8</sub><sup>2-</sup> system: reaction kinetics, degradation mechanism and acute toxicity, *Chem. Eng. J.* 339 (2018) 32–41, <https://doi.org/10.1016/j.cej.2018.01.106>.
- [60] W. Ben, Y. Shi, W. Li, Y. Zhang, Z. Qiang, Oxidation of sulfonamide antibiotics by chlorine dioxide in water: kinetics and reaction pathways, *Chem. Eng. J.* 327 (2017) 743–750, <https://doi.org/10.1016/j.cej.2017.06.157>.
- [61] A. Fabiańska, A. Biały-Bielinska, P. Stepnowski, S. Stolte, E.M. Siedlecka, Electrochemical degradation of sulfonamides at BDD electrode: kinetics, reaction pathway and eco-toxicity evaluation, *J. Hazard. Mater.* 280 (2014) 579–587, <https://doi.org/10.1016/j.jhazmat.2014.08.050>.
- [62] A.L. Boreen, W.A. Arnold, K. McNeill, Photochemical fate of sulfa drugs in the aquatic environment: sulfa drugs containing five-membered heterocyclic groups, *Environ. Sci. Technol.* 38 (2004) 3933–3940, <https://doi.org/10.1021/es0353053>.
- [63] S.P. Devi, R.H.D. Lyngdoh, Uncatalyzed gas phase aziridination of alkenes by organic azides. Part 2. Whole azide reaction with alkene, *J. Chem. Sci.* 131 (2019) 1–6, <https://doi.org/10.1007/s12039-018-1575-4>.
- [64] C. Ridruejo, F. Centellas, P.L. Cabot, I. Sirés, E. Brillas, Electrochemical Fenton-based treatment of tetracaine in synthetic and urban wastewater using active and non-active anodes, *Water Res.* 128 (2018) 71–81, <https://doi.org/10.1016/j.watres.2017.10.048>.
- [65] N. Oturan, S. Trajkovska, M.A. Oturan, M. Couderchet, J. Aaron, Study of the toxicity of diuron and its metabolites formed in aqueous medium during application of the electrochemical advanced oxidation process electro-Fenton, *Chemosphere* 73 (2008) 1550–1556, <https://doi.org/10.1016/j.chemosphere.2008.07.082>.
- [66] A. Dirany, I. Sirés, N. Oturan, A. Özcan, M.A. Oturan, Electrochemical treatment of the antibiotic sulfachloropyridazine: kinetics, reaction pathways, and toxicity evolution, *Environ. Sci. Technol.* 46 (2012) 4074–4082, <https://doi.org/10.1021/es204621q>.

Update

**Applied Catalysis B: Environmental**

Volume 271, Issue , 15 August 2020, Page

DOI: <https://doi.org/10.1016/j.apcatb.2019.117914>



Corrigendum

Corrigendum to “A biochar modified nickel-foam cathode with iron-foam catalyst in electro-Fenton for sulfamerazine degradation” [Appl. Catal. B: Environ. 256 (2019) 117796–117810]



Fengxia Deng<sup>a,b</sup>, Sixing Li<sup>b</sup>, Minghua Zhou<sup>c</sup>, Yingshi Zhu<sup>b</sup>, Shan Qiu<sup>b,\*</sup>, Kehong Li<sup>b</sup>, Fang Ma<sup>b</sup>, Jizhou Jiang<sup>c,d,\*</sup>

<sup>a</sup> State Key Laboratory of Urban Water Resources Center, School of Environment, Harbin Institute of Technology, Harbin 150090, PR China

<sup>b</sup> School of Chemical and Environmental Engineering, Jiang Han University, Wuhan 430056, PR China

<sup>c</sup> Key Laboratory of Pollution Process and Environmental Criteria, Ministry of Education, College of Environmental Science and Engineering, Nankai University, Tianjin 300350, China

<sup>d</sup> School of Environmental Ecology and Biological Engineering, Wuhan Institute of Technology, Wuhan 430205, PR China

<sup>e</sup> School of Materials Science and Energy Engineering, Foshan University, Foshan 528000, PR China

The authors regret < that in the above paper, by mistake the affiliations of authors are incorrect including Sixing Li, Yingshi Zhu, Shan Qiu, Kehong Li, Fang Ma. We would like to correct this error. The revised one is given as follows:

Fengxia Deng<sup>a, b</sup>, Sixing Li<sup>a</sup>, Minghua Zhou<sup>e</sup>, Yingshi Zhu<sup>a</sup>, Shan Qiu<sup>a,\*</sup>, Kehong Li<sup>a</sup>, Fang Ma<sup>a</sup>, Jizhou Jiang<sup>c,d,\*</sup>

<sup>a</sup> State Key Laboratory of Urban Water Resources Center, School of Environment, Harbin Institute of Technology, Harbin 150090, PR China

<sup>b</sup> School of Chemical and Environmental Engineering, Jiang Han

University, Wuhan 430056, PR China

<sup>c</sup> School of Environmental Ecology and Biological Engineering, Wuhan Institute of Technology, Wuhan 430205, PR China

<sup>d</sup> School of Materials Science and Energy Engineering, Foshan University, Foshan 528000, PR China

<sup>e</sup> Key Laboratory of Pollution Process and Environmental Criteria, Ministry of Education, College of Environmental Science and Engineering, Nankai University, Tianjin 300350, PR China > .

The authors would like to apologise for any inconvenience caused.

DOI of original article: <https://doi.org/10.1016/j.apcatb.2019.117796>

\* Corresponding author.

\*\* Corresponding author at: School of Environmental Ecology and Biological Engineering, Wuhan Institute of Technology, Wuhan 430205, PR China.

E-mail addresses: [qiushan@hit.edu.cn](mailto:qiushan@hit.edu.cn) (S. Qiu), [027wit@163.com](mailto:027wit@163.com) (J. Jiang).